Ferroelectricity in Untwisted Heterobilayers of Transition Metal Dichalcogenides by Chemical Vapour Deposition

Authors: *Lukas Rogée,[1,†] Lvjin Wang,[2,†] Yi Zhang,[1]Songhua Cai,[1] Peng Wang,[3] Manish Chhowalla,[4]* Wei Ji,[2,]* Shu Ping Lau[1,]**

Affiliations:

[1]Department of Applied Physics, The Hong Kong Polytechnic University, Hung Hom, Kowloon, Hong Kong SAR, P. R. China

[2]Department of Physics and Beijing Key Laboratory of Optoelectronic Functional Materials & Micro-Nano Devices, Renmin University of China, Beijing 100872, P. R. China

[3]College of Engineering and Applied Sciences and Collaborative Innovation Center of Advanced Microstructures, Nanjing University, Nanjing 210093, P. R. China

[4]Department of Materials Science & Metallurgy, University of Cambridge, Cambridge, UK

*Correspondence authors. Email: apsplau@polyu.edu.hk (SPL), E-mail: wji@ruc.edu.cn (WJ) and E-mail: mc209@cam.ac.uk (MC)

[†]LR and LW contributed equally to this work.

Abstract: Two-dimensional (2D) materials with out-of-plane (OOP) ferroelectric and piezoelectric properties are highly desirable for the realization of ultrathin ferro- and piezo-electronic devices. Here, we demonstrate unexpected OOP ferroelectricity and piezoelectricity in untwisted, commensurate and epitaxial MoS_2/WS_2 heterobilayers synthesized by scalable one-step chemical vapour deposition (CVD). We show d_{33} piezoelectric constants of $1.95 – 2.09$ pmV^{-1} that are larger than the natural OOP piezoelectric constant of monolayer In_2Se_3 by a factor of ~ 6. Further, we demonstrate the modulation of tunneling current by $\sim 10^3$ times in ferroelectric tunnel junction (FTJ) devices by changing the polarization state of MoS_2/WS_2 heterobilayers. Our results are consistent with density functional theory (DFT) which shows that both symmetry breaking and interlayer sliding give rise to the unexpected properties without the need for invoking twist angles or Moiré domains.

One-Sentence Summary: Two different 2D materials when stacked together show new properties that the individual materials lack.

Main Text:

The rational vertical integration of 2D materials has led to new and exciting condensed matter effects that have opened new avenues of research. These interesting effects are a consequence of novel interactions between the layers of atomically thin materials that give rise to Moiré superlattices, hybrid electronic structures and breaking of the usual crystal symmetries.(*1*) Materials such as graphene and bilayer 2H MoS_2 are centro-symmetric.(*2*) In contrast, odd numbers of layers of 2D materials such as MoS_2 are non-centrosymmetric, belonging to the $\bar{6}m2$ point group (or D_{3h}), and therefore exhibit in-plane (IP) piezoelectricity. Non-centrosymmetric 2D materials also generate second harmonic emission that can be used to confirm the absence of

inversion symmetry. The magnitude of the IP piezoelectric component, referred to as d_{11} (or d_{22} if the armchair direction of the lattice is indexed as 2*)*, has been estimated to be ~ 2.5 to 4 pmV^{-1} for single layer MoS$_2$.(*3*) $\bar{6}m2$ point group materials do not exhibit OOP piezoelectricity.(*4*)

OOP piezoelectricity in 2D materials has been reported in few-layered In$_2$Se$_3$[(*5*)] and by introducing chalcogen vacancies in MoTe$_2$.(*6*) Theoretical studies have explored the piezoelectric properties of TMDC alloys when assembled into vertical heterostructures.(*7*) Recently, ferroelectricity has been observed in twisted layers of hexagonal boron nitride (h-BN) and TMDCs.(*8, 9*) The origin of ferro- and piezo-electricity in twisted bilayers arises from formation of Moiré lattices and interlayer sliding.(*10*) Ferro- and piezoelectricity have also been observed in rhombohedral homobilayer TMDCs.(*11*) However, OOP piezoelectric and ferroelectric effects in epitaxially grown, untwisted, commensurately stacked, laterally large vertical heterostructures of 2D TMDCs have not been experimentally reported.

We have developed a simple one-step CVD process to grow commensurate MoS$_2$/WS$_2$ heterobilayers on SiO$_2$ substrates that possess measurable OOP ferroelectricity and an OOP piezoelectric component d_{33} – even though individual layers of WS$_2$ and MoS$_2$ have $d_{33} = 0$. This observation is explained by taking the heterobilayer to be one crystal system with its own point group. In the case of CVD-grown MoS$_2$/WS$_2$ heterobilayers studied here, the point group is $3m$ (or C_{3v}), which lacks the vertical symmetry to nullify OOP strain effects and thus possess a non-zero d_{33} component that has a magnitude of up to 2.09 pmV^{-1}. A special sub-group of piezoelectrics are also ferroelectric – that is, their internal electric polarization can be switched between two stable states via an external electric field. Ordinary 2D TMDCs are not known to exhibit any ferroelectric characteristics.(*12*) The classification of MoS$_2$/WS$_2$ heterobilayers as *3m* point group materials suggests that they could be ferroelectric. We confirm this via piezoresponse

measurements at room temperature. We demonstrate FTJs based on MoS_2/WS_2 heterobilayers, which use the switchability of the ferroelectric to control the tunneling current density through the device.(*13*)

An optical image of CVD-grown heterobilayers is shown in Figure 1. The image shows smaller WS_2 triangles (lateral dimensions of ~ 10 µm) draped by a larger MoS_2 monolayer (lateral dimensions of up to 200 µm). The details of the growth method are given in the Supplementary Materials (SM) Sections 1 and 2. Detailed Raman analysis from different regions on the sample, shown in Figure 1(B), shows pure single layer MoS_2 (region labeled as α, IP vibrational mode E' at ~ 383 cm^{-1} and the OOP vibrational mode A'_1 at ~ 403 cm^{-1}). The triangles labeled with β show Raman signals from both MoS_2 and WS_2 (E' mode of WS_2 at ~ 355 cm^{-1} and its A'_1 mode at ~ 417 cm^{-1} along with the MoS_2 peaks). In Figure 1(C), a scanning electron microscope (SEM) image of a large MoS_2 layer covering a smaller WS_2 triangle is shown. Cross-sectional high annular angle dark field scanning transmission electron microscope (HAADF-STEM) images from two regions labeled as (D), and (E) in Figure 1(C) were obtained. In the cross-sectional STEM images, MoS_2 and WS_2 can be easily distinguished by the higher contrast of the W atoms that make the WS_2 layer noticeably brighter than the MoS_2 layer. Bright-field STEM (BF-STEM) images provide additional evidence of the bilayer structure as shown in the SM Section 3. Chemical analysis of the heterobilayers using energy dispersive X-ray spectroscopy (EDS) confirmed the chemical composition of the heterobilayers – as shown in SM Section 4. In Figure 1(D), the larger MoS_2 layer draping over the edge of the WS_2 layer is clearly visible. In Figure 1(E), an MoS_2 layer on top of WS_2 can be clearly seen. Additional photoluminescence (PL) and selected area electron diffraction (SAED) data about the CVD grown materials can be found in SM Section 5.
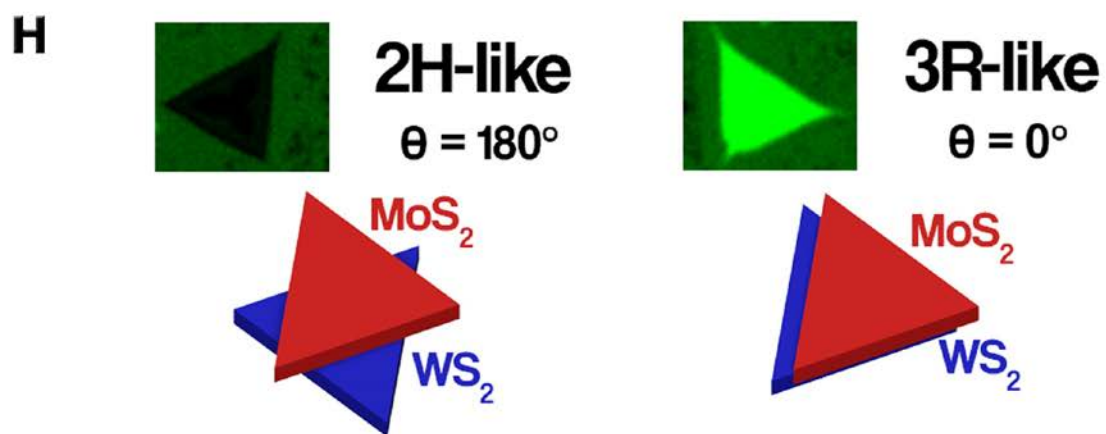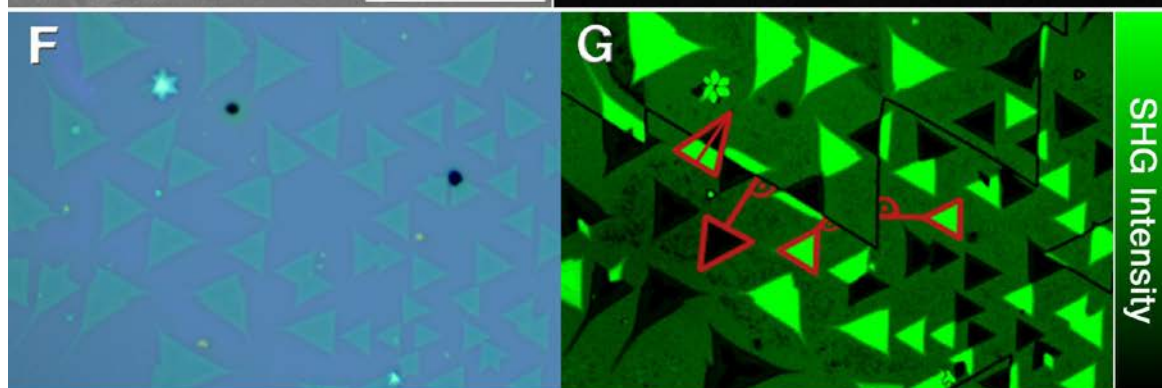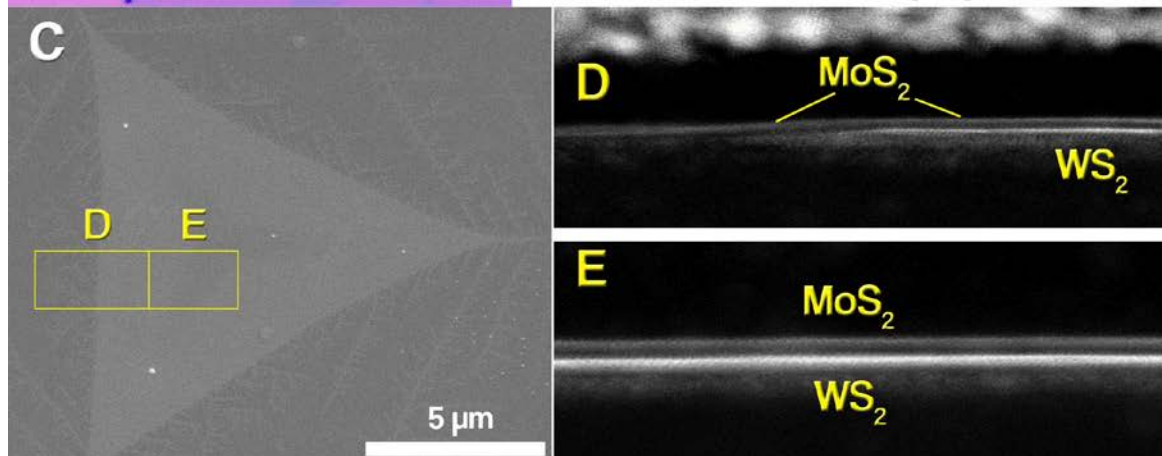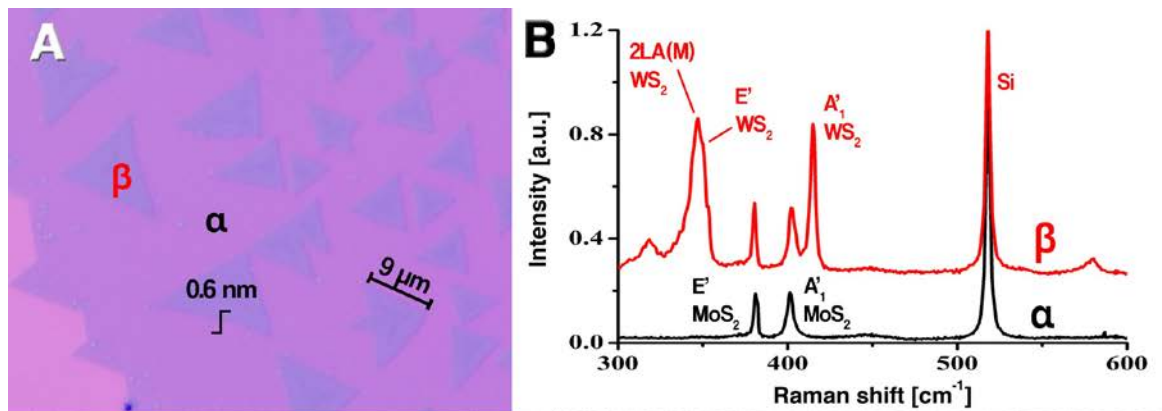
Fig. 1. CVD-grown MoS_2/WS_2 heterobilayers. (**A**) Optical microscope image of the as-grown heterobilayers showing smaller (~ 10 µm) WS_2 triangles draped over by a larger (~ 200 µm) MoS_2 layer. The thicknesses of the triangle edges were measured to be 0.6 nm by AFM – the thickness of a TMDC monolayer. (**B**) Raman spectra from α and β regions labeled in (A). α regions show typical MoS_2 signals, while β region shows both WS_2 and MoS_2 peaks. (**C**) Planar SEM image of a typical as-grown triangle. The two yellow squares indicate regions selected for cross-sectional STEM imaging. (**D, E**) Cross-sectional HAADF-STEM images. In region D, the MoS_2 layer draping over the brighter WS_2 layer is observed. In region E, a uniform bilayer consisting of MoS_2 on top of WS_2 can be seen. (**F**) Optical microscopy image of MoS_2/WS_2 triangles across a large MoS_2 cluster with the corresponding unfiltered SHG intensity map in (**G**). Note that there is no bare SiO_2 substrate visible in the image. The MoS_2/WS_2 triangles appear either very bright or very dark across the map. The black lines are single crystal domain boundaries of the large MoS_2 monolayer. Bright triangles always point toward the nearest domain boundaries, dark triangles point away from them as indicated by the red lines. (**H**) Relationship between SHG intensity and vertical stacking angle θ. Dark triangles are labeled 2H-like and bright triangles 3R-like.

We have studied the stacking angle between MoS_2 and WS_2 by second harmonic generation (SHG) emission, which depends directly on the inter-layer rotation angle θ.(*14*) MoS_2 and WS_2 exhibit broad absorption at energies above 2.5 eV,(*15*) and thus incident photons with a wavelength of 900 nm (1.37 eV) readily induce SHG emissions of 450 nm (2.74 eV) in both layers. The SHG map of our CVD grown heterobilayers is shown in Figure 1(G). In short, SHG emissions interfere entirely constructively (bright signal) when $\theta = 0°$ where the stacking sequence is similar to the 3R stacking in TMDC crystals, as shown schematically in Figure 1(H). Conversely, when the stacking angle is $\theta = 60°$ (or 180°, 300° and so on because of 3-fold rotation symmetry of TMDCs around the c-axis) as in the 2H phase TMDCs, the layers interfere entirely destructively and produce a dark signal. Additional information about SHG and heterobilayer geometry and the corresponding STEM analysis are provided in SM Sections 6 and 7.

Vertical bilayer heterostructures are often associated with the appearance of Moiré patterns, which can have a significant impact on their piezo- and ferroelectric properties. In our case, the epitaxial heterobilayers do not show any Moiré patterns as we show in SM Section 8. Briefly,

naturally grown bilayer TMDCs in either 2H or 3R stacking do not show Moiré superlattices because their layers are commensurate. This is not exclusive to homobilayers. MoS_2 and WS_2 have virtually identical lattice parameters(*15, 16*) and as a consequence, heterobilayers of MoS_2 and WS_2 with a twist angle of $n \cdot 60$ ° (with *n* being an integer) also do not show Moiré superlattices. Our heterobilayers grown by CVD naturally align with each other in energetically ideal arrangements, i.e. epitaxially – consistent with epitaxially grown WSe_2/$MoSe_2$ heterobilayers(*17*) that also show an absence of Moiré patterns because they also possess identical lattice constants. Commensurate stacking of different TMDC monolayers cannot yet be achieved by artificial stacking. A small difference in lattice constant between MoS_2 and WS_2 of 0.01 Å has been reported but studies have shown that heterobilayers with lattice constant differences of up to 2 % can become commensurate during the CVD growth.(*18*) An example is CVD-grown monolayer graphene on Ni(111) which despite a small lattice mismatch reproduce a 1x1 commensurate hetero-lattice.

The STEM image in Figure S9(A) shows the edge of two heterobilayers with the same orientation. At this scale, edges of Moiré patterns would become apparent in artificially stacked bilayers with small stacking angles. However, this is not the case for CVD samples. The corresponding FFT spectrum of the image shows a single hexagonal crystal pattern, similar to the SAED pattern shown in Figure S6(D). Figure S9(B) shows the STEM image of 3R-like and 2H-like heterobilayers. Moiré patterns are also absent in this sample. The FFT spectra for the entire image, the 3R-like and 2H-like stacked heterobilayers along with that of only MoS_2 are also shown. All FFT spectra are the same, which suggest no misalignment or twisting between the two layers. We therefore do not need to invoke twisting or Moiré lattices to describe the origins of piezo- and ferroelectricity in our CVD grown heterobilayers.
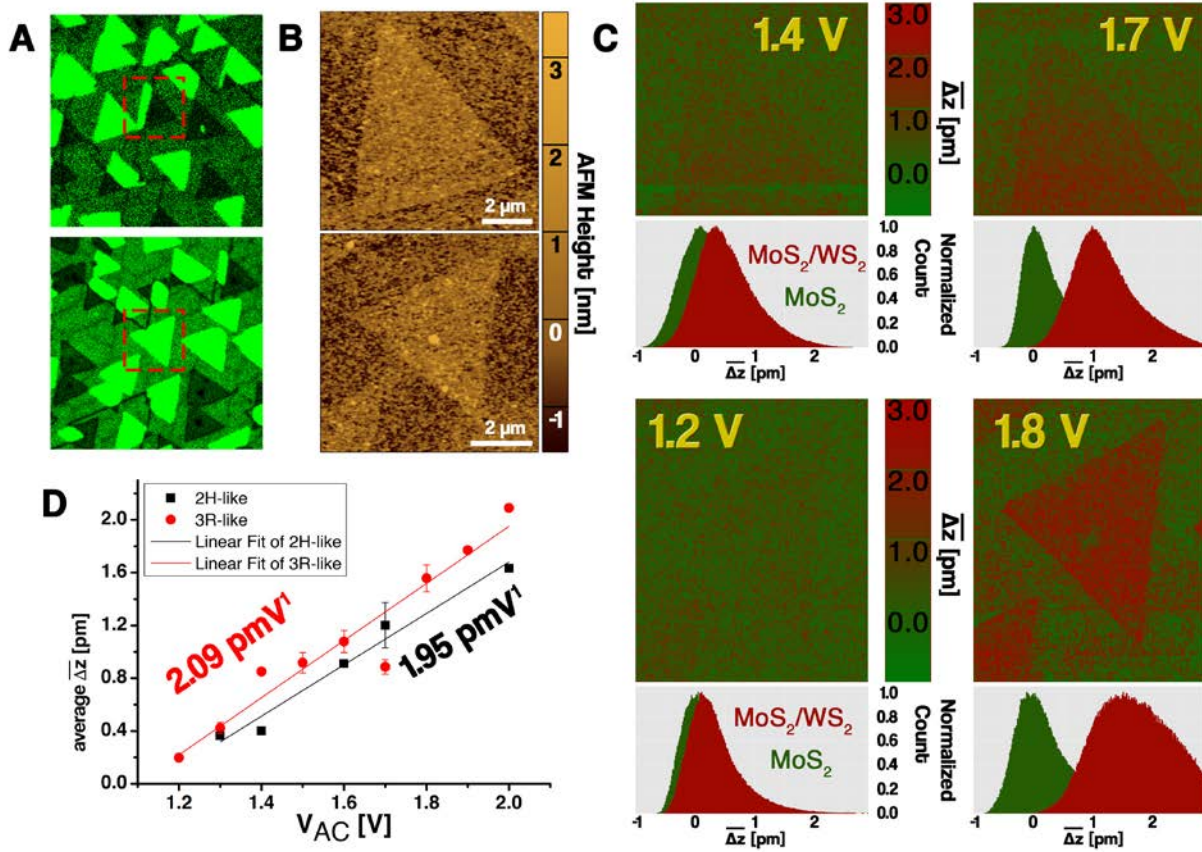
Fig. 2. PFM data of MoS$_2$/WS$_2$ heterobilayers on a conductive Pt coated substrate. (**A**) SHG maps showing the triangles that were chosen for the PFM measurements. The upper triangle is largely 2H-like. The lower triangle is 3R-like. (**B**) AFM maps of the 2H-like and 3R-like triangles. The materials are atomically smooth with RMS roughness of ~ 0.1nm. (**C**) Real piezoelectric height change $\overline{\Delta z}$ maps of both triangles, measured at different drive voltages, V_{AC}. The distributions below each map show the piezoelectric height change for the MoS$_2$/WS$_2$ triangles (red) and the surrounding monolayer MoS$_2$ (green). (**D**) Plot of the average values of $\overline{\Delta z}$ as a function of V_{AC}.

Piezoelectric mapping. Both 3R-like and 2H-like MoS$_2$/WS$_2$ heterobilayers can be treated as materials belonging to the $3m$ (or C_{3v}) point group that should exhibit a non-zero OOP piezoelectric constant d_{33} and be potentially ferroelectric. We have therefore investigated both properties using piezoresponse force microscopy (PFM) (DART-SS-PFM mode, Asylum Research, see Methods).(*19*) In short, an alternating electric field (at voltage V_{AC}) is created locally using a conductive AFM tip, which causes piezoelectric materials to deform; the magnitude of the

deformation is measured and mapped. For PFM measurements, heterobilayers were transferred onto conductive substrates to avoid electrical charging during the measurements. Figure 2(A) shows the SHG maps of triangles with different vertical stacking arrangements, and their corresponding atomic force microscopy (AFM) images are shown in Figure 2(B). The two different stacking arrangements of MoS_2/WS_2 heterobilayers appear very similar in the AFM. We performed resonance amplified PFM to obtain the OOP piezoelectric constant. The mapping results at different voltages between 1.2 and 2.0 V are shown in Figure 2(C). The colour scale of the PFM maps has been set such that the mean height change of the pure MoS_2 is zero, and its colour is green. This helps to account for possible electrostrictive effects from the background since MoS_2 by itself does not exhibit OOP piezoelectricity. The results in Figure 2(C) show that with increasing voltage, the colour contrast between the MoS_2/WS_2 heterobilayer and the pure MoS_2 monolayer significantly increases. That is, significant OOP piezoelectricity is indicated by the red colour in the PFM maps. The average of the vertical piezoelectric deformation $\overline{\Delta z}$ of multiple 2H-like and 3R-like triangles was obtained by rigorous statistical analysis to find the piezoelectric height change on the vertical heterostructures relative to the background (SM Section 9). The $\overline{\Delta z}$ distributions for both the background and heterobilayers plotted below each PFM map show that the distance between the background and triangle distributions increases with increasing voltage, as we would expect for OOP piezoelectricity. Also, the distribution for the triangles get broader. This is because the real value of d_{33} varies slightly across the area of a triangle, and these slight differences multiplied by an increasing voltage V_{AC} result in ever greater contrast between the extremes of $\overline{\Delta z}$. We have plotted the average of $\overline{\Delta z}$ as a function of V_{AC} for both stacking types in Figure 2(D) along with their respective linear fits.

Material	Piezoelectric Constant	Experimental Value [pmV^{-1}]
2H-like MoS$_2$/WS$_2$	d_{33}	1.95
3R-like MoS$_2$/WS$_2$	d_{33}	2.09
Monolayer MoS$_2$ [(20)]	d_{11}	3.78
Monolayer WSe$_2$ [(21)]	d_{11}	5.2
Monolayer α-In$_2$Se$_3$ [(5)]	d_{33}	0.34

Table 1. Overview over several notable 2D materials and their measured piezoelectric constants.

The OOP piezoelectric component can be calculated using $d_{33} = \frac{\partial(\overline{\Delta z})}{\partial V_{AC}}$. We find $d_{33} = 1.95 \pm 0.2$ pmV^{-1} and 2.09 ± 0.2 pmV^{-1} for 2H-like and 3R-like stacked MoS$_2$/WS$_2$, respectively. For comparison, experimentally obtained piezoelectric constants of other 2D materials are shown in Table 1. We find that our measured data are similar in magnitude to the IP d_{11} piezoelectric constant of monolayer MoS$_2$ and significantly larger than the OOP d_{33} constant of monolayer α-In$_2$Se$_3$.(5) We also see that the stacking orientation of the heterostructure has a slight influence on its piezoelectric constant. Due to the difference in stacking, the relative positions of W, Mo, and S atoms are different, which ultimately influences the magnitude and direction of the internal polarization. Spurious OOP piezoelectric effects can arise when the root mean square (RMS) roughness is higher than the thickness of TMDCs (>1.5 nm).(22) The AFM images in Figure 2(B) show that this is not the case in our samples because the heterobilayers are atomically smooth with RMS surface roughness of ~ 0.1 nm. This value is considerably less than the thickness of the heterobilayer, hence the OOP deformation reported here is intrinsic.
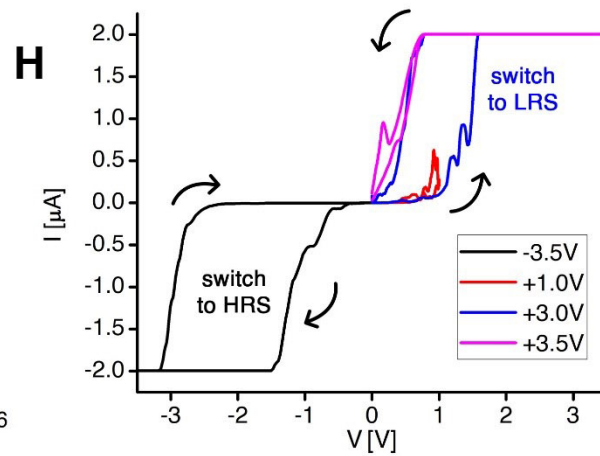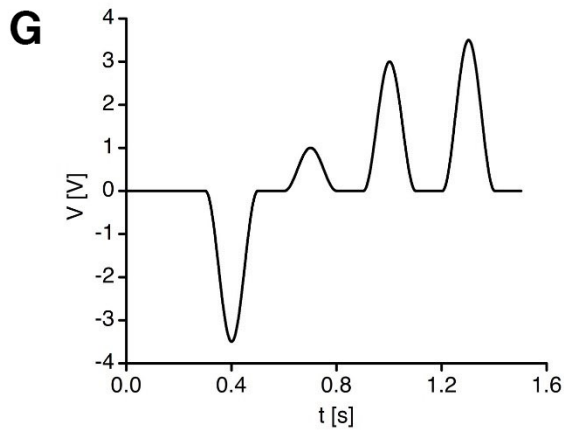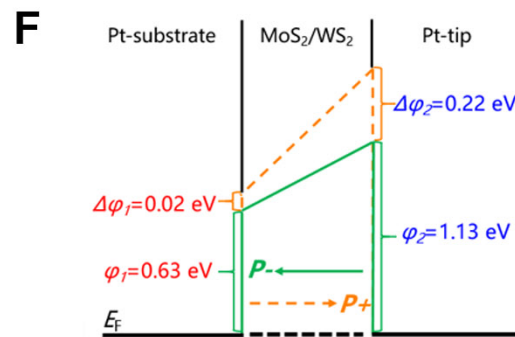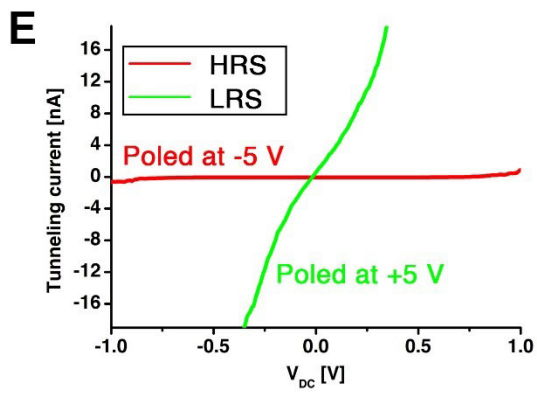
A — V_DC OFF
B — V_DC ON
C — unpoled
D — unpoled
E — HRS / LRS / Poled at -5 V / Poled at +5 V
F — Pt-substrate / MoS₂/WS₂ / Pt-tip / $\Delta\varphi_2 = 0.22$ eV / $\Delta\varphi_1 = 0.02$ eV / $\varphi_2 = 1.13$ eV / $\varphi_1 = 0.63$ eV / P_- / P_+ / E_F
G
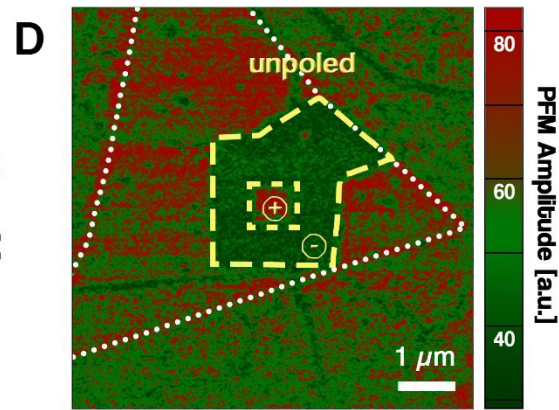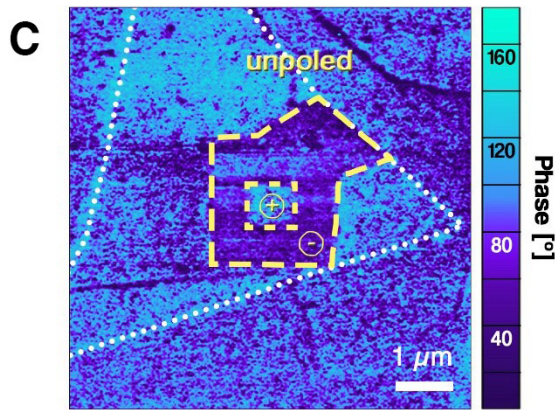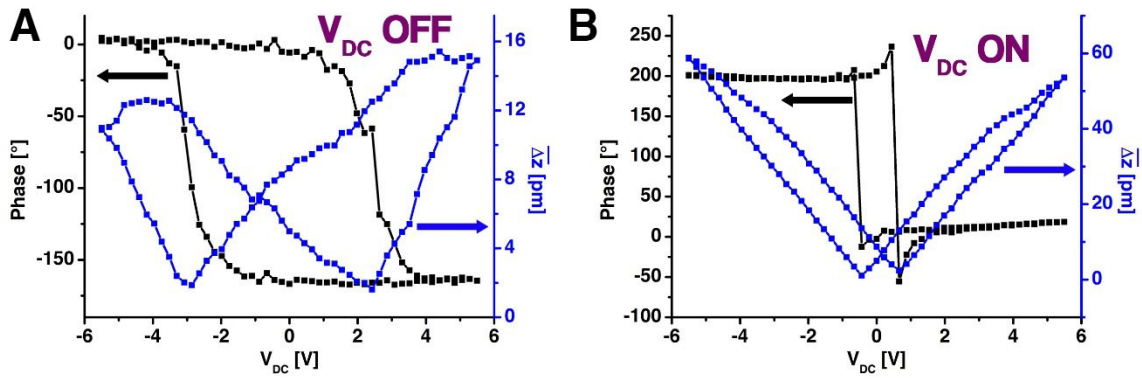H — switch to LRS / switch to HRS / -3.5V / +1.0V / +3.0V / +3.5V

Fig. 3. Ferroelectricity in MoS_2/WS_2 heterobilayers. Piezoelectric hysteresis loops were measured by applying DC voltage sweeps from –5.5 to +5.5 V at 2.7 V AC drive voltage using DART-SS-PFM. (**A**) Phase and $\overline{\Delta z}$ hysteresis loops with the DC field OFF. (**B**) Phase and $\overline{\Delta z}$ hysteresis loops with the DC field ON. (**C, D**) Two square-shaped domains were written onto a heterobilayer triangle with -8 V for the outer square and 8 V for the inner square. The entire triangle is outlined by the dotted white line for clarity. The phase map (C) and PFM amplitude map (D) show that the poled areas, marked by dashed yellow outlines, do not extend beyond the boundaries. (**E**) Polarization dependent tunneling current versus applied DC field through an FTJ device. The tunneling current is strongly dependent on the previous poling voltage. The ratio between the low and high resistance states (LRS and HRS) is 10^2 to 10^3. The tunneling potential barrier change for the LRS and HRS states for an FTJ are schematically represented in (**F**). Electron tunneling is reduced when the device is poled with a negative voltage, and increased with a positive poling voltage. (**G**) Switching voltage programme applied to an FTJ for more in-depth analysis. A negative poling voltage pulse of -3.5 V is applied, followed by three positive voltage pulses with increasing magnitudes of 1 V, 3 V and 3.5 V. The corresponding I-V loop is shown in (**H**). The arrows indicate the direction of the current change.

Ferroelectric hysteresis. The observation of a piezoelectric response in MoS_2/WS_2 heterobilayers does not necessarily imply the presence of ferroelectricity; however, the $3m$ point group classification indicates that it is possible.(*12, 23*) Room-temperature ferroelectricity in stacked large area CVD grown TMDCs would open up the possibilities for exciting new electronics applications. We thus investigated the ferroelectric response of the heterobilayers. The results are shown in Figure 3. First, we applied the DART-SS-PFM hysteresis method to our sample as described in the Methods section. The OFF-field phase loop in Figure 3(A) shows the typical shape obtained from domain switching in ferroelectric materials. It is apparent that the polarization switching occurs at the coercive voltage of $\sim V_{DC} = \pm 3$ V in the heterobilayers. The corresponding OFF-field $\overline{\Delta z}$ loop exhibits the typical ferroelectric butterfly shape. Generally, the OFF-field piezoresponse hysteresis loops are used to investigate the ferroelectric performance to avoid spurious electrostrictive and electrochemical forces that can otherwise also cause piezoresponse loops that appear similar to ferroelectric ones.(*24*) The butterfly loop is slightly offset toward the negative voltage direction. This is indicative of small influences from non-ferroelectric artifacts,

such as charge injection – a common feature in ultra-thin ferroelectrics.(*25*) Figure 3(B) shows the corresponding ON-field hysteresis loops. A phase loop is also apparent here although it is more abrupt. The ON-field $\overline{\Delta z}$ loop appears as a large V-shape with a small butterfly pattern. These two shapes show that the ferroelectric and electrostrictive deformation co-exist as long as a strong unidirectional electric field is present. Some non-ferroelectric materials like Al_2O_3 exhibit piezoresponse hysteresis loops even in OFF-field loops, which can be mistaken to be of ferroelectric origin.(*26, 27*) In SM Section 10, we show through variation of the drive voltage V_{AC} that the observed ferroelectricity is intrinsic. Further evidence of ferroelectricity is provided through domain writing (see Methods). We poled a large area of the heterobilayer (with -8 V tip bias) and a smaller square within that area (+8 V tip bias). These shapes are outlined in the phase and amplitude maps performed after poling as shown in Figures 3(C, D). They show a strong change in both the phase direction as well as the PFM amplitude in the designated areas.

To translate the fundamental ferroelectric properties into a practical demonstration, we measured the properties of FTJ devices based on the heterobilayers. The V_{DC}-dependent tunneling current in a FTJ can be substantially modified by poling the device prior to measurements, as shown in Figure 3(E). The device characteristics are also similar to ferrodiode behaviour as reported by Liu *et al.*.(*28*) Thus, while we use the term FTJ to describe our device, additional work is required to distinguish between the two. In this case, negative poling with -5 V diminishes the electron tunneling current and puts the device in a high-resistance-state (HRS), whereas positive poling of +5 V put it in a low-resistance-state (LRS); the ratio of the tunneling resistance between the two states reaches a value of 10^2 to 10^3. Figure 3(F) shows schematically how modification of the tunnel barrier with polarization of the ferroelectric (*13, 29-31*) increases or decreases the tunneling current.(*32, 33*) We have included a more detailed theoretical discussion regarding the

tunnel barrier modification to SM Section 11. Further, we have repeatedly applied a resistance switching voltage programme to an FTJ as shown in Figure 3(G) to test for robustness. For each measurement cycle, a strong negative voltage pulse (-3.5 V) is applied to the sample to ensure that it is poled in the HRS. Then, three positive voltage pulses of 1 V, 3 V and 3.5 V are applied. The resulting tunneling current measurements (Figure 3(H)) show that the negative voltage induces HRS. The application of the 1 V pulse increases and decreases the current along the HRS curve, without forming an open loop. Once the 3 V pulse is applied an open loop is created where the sample switches from HRS to LRS, and the 3.5 V pulse simply follows the LRS curve without any open loop, since resistance switching has already occurred. These measurements confirm that a voltage of at least the coercive voltage is needed to switch between the FTJ states, in accordance with the PFM data from Figure 3(A). In SM Section 12, we show more detailed poling experimental data on the same and other devices. Our overall hysteresis results indicate that MoS_2/WS_2 heterobilayers, as a *3m* point group material, exhibit ferroelectric properties at room temperature.
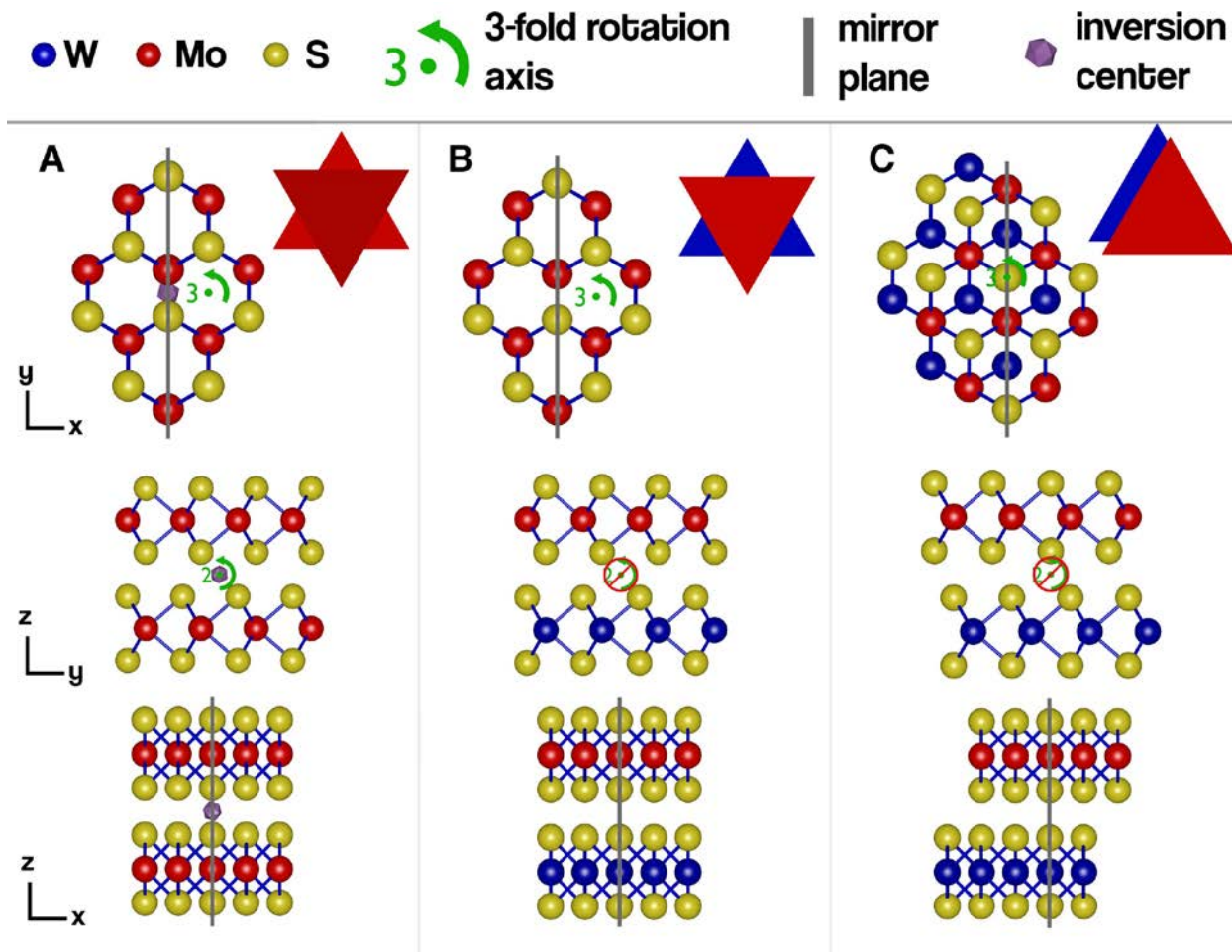
Fig. 4. Schematic representation of (**A**) bilayer 2H MoS$_2$, (**B**) 2H-like and (**C**) 3R-like heterostructure of MoS$_2$/WS$_2$ from three different perspectives as indicated by the coordinate axes. The c-direction (OOP direction) is along the z-axis, the zig-zag direction is along the x-axis, the armchair direction is along the y-axis.

Crystal symmetries. In this section, we discuss the relationship between our experimental observations and crystal symmetry considerations based on Group Theory. Detailed tensor mathematics and explanations can be found in SM Section 13. TMDCs are known to show IP piezoelectric properties but no OOP piezoelectric properties.(*4, 34*) Bilayer 2H MoS$_2$ belongs to the $\bar{3}\frac{2}{m}$ (or *D$_{3d}$*) point group. A schematic model of its crystal structure is depicted in Figure 4(A), which notably includes an inversion centre. Inversion centres are central for ferro- and piezoelectricity (also for SHG), which do not occur if an inversion centre is present in a crystal. In

Figure 4(B), a schematic of the 2H-like MoS_2/WS_2 heterobilayer is shown. The crystal is like

bilayer 2H MoS_2 with the exception that Mo atoms are replaced with W atoms in the bottom layer.

This makes a significant difference to the crystal symmetry but does not lead to appearance of

Moiré patterns due to the similarity in lattice parameters of the two materials and their epitaxial

growth. Now all symmetry transformations that exchange atoms between the top and bottom layers

become invalid, including the inversion centre. The symmetry transformations that are left put the

heterobilayer into the $3m$ (or C_{3v}) point group. The same symmetry transformations also apply for

3R-like MoS_2/WS_2 as depicted in Figure 4(C); hence both stacking types belong to the same point

group. The $3m$ point group has exactly one non-zero OOP piezoelectric constant called d_{33}. $3m$

point group materials also classify as polar materials because they have a unique rotation axis, no

inversion centre, and no mirror plane perpendicular to the rotation axis.(*12*) As such, from a

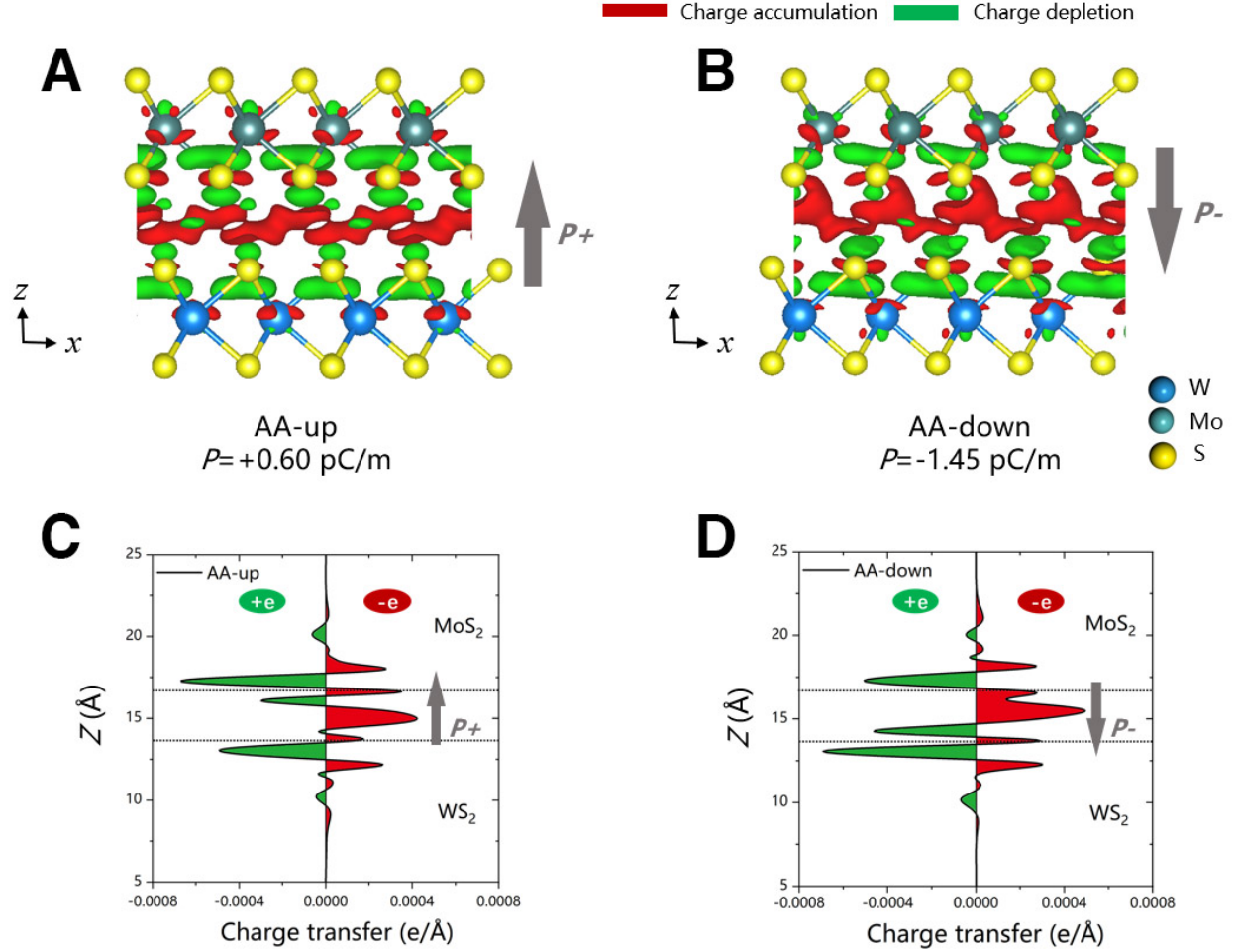geometric standpoint, ferroelectricity is possible.

Fig. 5: Plot of interlayer differential charge density for the up (**A**, AA-up) and down (**B**, AA-down) polarizations. An iso-surface value of 7×10^{-5} e/bohr^3 was used. Their line profiles along z were plotted in (**C**) and (**D**), respectively.

Theoretical derivation of strain-piezoelectric constant and mechanism of ferroelectric switching. The strain-piezoelectric constant (d), measured in our experiments, cannot be directly obtained from DFT calculations. However, it could be derived from the stress-piezoelectric constant (e) and the elastic constant tensor (C) using relation $d = eC^{-1}$, which are obtainable from DFT calculations. The OOP component of the strain piezoelectric constant tensor d_{33}, as measured in our PFM experiment, is theoretically derived from $d_{33} = [(C_{11} + C_{12})e_{33} - 2C_{13}e_{31}]/[(C_{11} + C_{12})C_{33} - 2C_{13}^2]$ (see SM Section 14).

The vertical strain piezoelectric constants of 2H-like and 3R-like MoS_2/WS_2 heterobilayers were determined to be 2.28 pmV^{-1} and 2.40 pmV^{-1}. Both these absolute values of the two d_{33} constants, i.e. 2.28 and 2.40 pmV^{-1}, and their difference, i.e. 0.12 pmV^{-1}, are very close to experimentally measured value, i.e. 1.95, 2.09 and 0.14 pmV^{-1}, respectively.

According to our calculations, both heterobilayers show spontaneous non-zero OOP electric polarizations, namely P_{out}[2H-like] = 0.44 pC·m^{-1} and P_{out}[3R-like] = 0.60 pC·m^{-1}. Switching their OOP polarization directions is not likely to be accessible by vertically moving any atoms, but could be achieved by a lateral sliding between the two monolayers in each of the heterobilayers, showing ferroelectric behaviour. SM Section 15 shows the atomic structures of two stacking configurations, i.e. AA-up and AA-down, of the 3R-like heterobilayer, which differ from one another by a 1.83 Å lateral sliding along the armchair direction. Configuration AA-up, showing an OOP polarization of 0.60 pC·m^{-1}, is 1.9 meV/f.u. more stable than configuration AA-down, which yields a negative value of -1.45 pC·m^{-1}. An external electric field over 2.4 V/nm could switch their relative stability and thus, together with thermal exciation at finite temperatures, trigger the sliding occurrence surmounting a 16 meV/f.u. barrier, which accompanies reversal of polarization direction, displaying an explicit ferroelectric switching behavior.

The interfacial differential charge densities (DCD, represents charge variation at the interface) of two related AA-like (i.e. 3R-like for our particular case) stacking configurations of the heterobilayers are shown in Figure 5. They explicitly show charge redistribution between the top and bottom layers that are illustrated as separation of the red (electron accumulation) and green (electron depletion) regions. Their line-profiles show explicit electric polarization at the interfaces and the direction of polarization is switchable under lateral sliding of one layer across roughly 1/3 of the unit cell. Our calculations give a switching barrier of 16 meV/f.u..This is comparable to the

value of 9 meV/f.u. predicted by Li *et al.*(*35*) in BN bilayers where the sliding mechanism was used. This mechanism was also used to explain those experimentally observed ferroelectric effects by Stern *et al.*(*10*) and Yasuda *et al.*(*9*) in a temperature range from 4.2 K to 300 K.

Conclusion. In this work, we demonstrate that ferro- and piezoelectricity can be found in untwisted commensurate bilayers consisting of monolayers of MoS_2 and WS_2. The experimental results can be explained by Group Theory without invoking Moiré lattices or domains.

References and Notes

1. A. Weston *et al.*, Atomic Reconstruction in Twisted Bilayers of Transition Metal Dichalcogenides. *Nat. Nanotechnol.* **15**, 592-597 (2020). doi:10.1038/s41565-020-0682-9
2. S. Islam, S. S. Z. Ashraf, Point and Space Groups of Graphene. *Reson* **24**, 445-457 (2019). doi:10.1007/s12045-019-0797-1
3. C. Cui, F. Xue, W.-J. Hu, L.-J. Li, Two-Dimensional Materials With Piezoelectric and Ferroelectric Functionalities. *npj 2D Mater. Appl.* **2**, 18 (2018). doi:10.1038/s41699-018-0063-5
4. A. H. Meitzler, IEEE Standard on Piezoelectricity. *ANSI/IEEE Std 176-1987*, 0_1 (1988). doi:10.1109/IEEESTD.1988.79638
5. F. Xue *et al.*, Multidirection Piezoelectricity in Mono- and Multilayered Hexagonal α-In_2Se_3. *ACS Nano* **12**, 4976-4983 (2018). doi:10.1021/acsnano.8b02152
6. D. Seol *et al.*, Selective Patterning of Out-of-Plane Piezoelectricity in $MoTe_2$ via Focused Ion Beam. *Nano Energy* **79**, 105451 (2021). doi:10.1016/j.nanoen.2020.105451
7. S. Yu, Q. Rice, B. Tabibi, Q. Li, F. J. Seo, Piezoelectricity in WSe_2/MoS_2 Heterostructure Atomic Layers. *Nanoscale* **10**, 12472-12479 (2018). doi:10.1039/c8nr04394a
8. A. Weston *et al.*, Interfacial Ferroelectricity in Marginally Twisted 2D Semiconductors. *arXiv [cond-mat.mes-hall]*, (2021).
9. K. Yasuda, X. Wang, K. Watanabe, T. Taniguchi, P. Jarillo-Herrero, Stacking-Engineered Ferroelectricity in Bilayer Boron Nitride. *Science* **372**, 1458-1462 (2021). doi:10.1126/science.abd3230
10. M. V. Stern *et al.*, Interfacial Ferroelectricity by Van Der Waals Sliding. *Science* **372**, 1462-1466 (2021). doi:10.1126/science.abe8177
11. X. Wang *et al.*, Interfacial Ferroelectricity in Rhombohedral-Stacked Bilayer Transition Metal Dichalcogenides. *Nat. Nanotechnol.*, (2022). doi:10.1038/s41565-021-01059-z
12. P.-P. Shi *et al.*, Symmetry Breaking in Molecular Ferroelectrics. *Chem. Soc. Rev.* **45**, 3811-3827 (2016). doi:10.1039/C5CS00308C
13. P. Hou *et al.*, An Ultrathin Flexible Electronic Device Based on the Tunneling Effect: A Flexible Ferroelectric Tunnel Junction. *J. Mater. Chem. C* **6**, 5193-5198 (2018). doi:10.1039/C8TC00500A

14. W.-T. Hsu *et al.*, Second Harmonic Generation from Artificially Stacked Transition Metal Dichalcogenide Twisted Bilayers. *ACS Nano* **8**, 2951-2958 (2014). doi:10.1021/nn500228r

15. R. A. Bromley, R. B. Murray, A. D. Yoffe, The Band Structures of Some Transition Metal Dichalcogenides. III. Group Via: Trigonal Prism Materials. *J. Phys. Condens. Matter* **5**, 759-778 (1972). doi:10.1088/0022-3719/5/7/007

16. A. Molina-Sánchez, L. Wirtz, Phonons in Single-Layer and Few-Layer MoS_2 and WS_2. *Phys. Rev. B* **84**, 155413 (2011). doi:10.1103/PhysRevB.84.155413

17. W.-T. Hsu *et al.*, Negative Circular Polarization Emissions From WSe_2/$MoSe_2$ Commensurate Heterobilayers. *Nat. Commun.* **9**, 1356 (2018). doi:10.1038/s41467-018-03869-7

18. Y. Dedkov, E. Voloshina, M. Fonin, Scanning Probe Microscopy and Spectroscopy of Graphene on Metals. *Phys. Status Solidi B* **252**, 451-468 (2015). doi:10.1002/pssb.201451466

19. R. Proksch, S. Kalinin, *Piezoresponse Force Microscopy with Asylum Research AFMs*. (Asylum Research).

20. S. K. Kim *et al.*, Directional Dependent Piezoelectric Effect in CVD Grown Monolayer MoS_2 for Flexible Piezoelectric Nanogenerators. *Nano Energy* **22**, 483-489 (2016). doi:10.1016/j.nanoen.2016.02.046

21. E. Nasr Esfahani, T. Li, B. Huang, X. Xu, J. Li, Piezoelectricity of Atomically Thin WSe_2 via Laterally Excited Scanning Probe Microscopy. *Nano Energy* **52**, 117-122 (2018). doi:10.1016/j.nanoen.2018.07.050

22. S. Kang *et al.*, Tunable Out-of-Plane Piezoelectricity in Thin-Layered $MoTe_2$ by Surface Corrugation-Mediated Flexoelectricity. *ACS Appl. Mater. Interfaces* **10**, 27424-27431 (2018). doi:10.1021/acsami.8b06325

23. D. Litvin, Ferroelectric Space Groups. *Acta Crystallogr. A* **42**, 44-47 (1986). doi:10.1107/S0108767386099920

24. B. Kim, D. Seol, S. Lee, H. N. Lee, Y. Kim, Ferroelectric-Like Hysteresis Loop Originated From Non-Ferroelectric Effects. *Appl. Phys. Lett.* **109**, 102901 (2016). doi:10.1063/1.4962387

25. S. S. Cheema *et al.*, Enhanced Ferroelectricity in Ultrathin Films Grown Directly on Silicon. *Nature* **580**, 478-482 (2020). doi:10.1038/s41586-020-2208-x

26. Z. Guan *et al.*, Identifying Intrinsic Ferroelectricity of Thin Film With Piezoresponse Force Microscopy. *AIP Adv.* **7**, 095116 (2017). doi:10.1063/1.4999199

27. H. Qiao, O. Kwon, Y. Kim, Electrostatic Effect on Off-Field Ferroelectric Hysteresis Loop in Piezoresponse Force Microscopy. *Appl. Phys. Lett.* **116**, 172901 (2020). doi:10.1063/5.0004532

28. X. Liu *et al.*, Aluminum Scandium Nitride-Based Metal–Ferroelectric–Metal Diode Memory Devices With High on/off Ratios. *Appl. Phys. Lett.* **118**, 202901 (2021). doi:10.1063/5.0051940

29. R. Li *et al.*, Preparation and Characterization of a Flexible Ferroelectric Tunnel Junction. *Appl. Phys. Lett.* **116**, 222904 (2020). doi:10.1063/5.0006638

30. J. Wu *et al.*, High Tunnelling Electroresistance in a Ferroelectric Van Der Waals Heterojunction via Giant Barrier Height Modulation. *Nat. Electron.* **3**, 466-472 (2020). doi:10.1038/s41928-020-0441-9

31. S. Yuan *et al.*, Room-Temperature Ferroelectricity in $MoTe_2$ Down to the Atomic Monolayer Limit. *Nat. Commun.* **10**, 1775 (2019). doi:10.1038/s41467-019-09669-x

32. E. Y. Tsymbal, H. Kohlstedt, Tunneling Across a Ferroelectric. *Science* **313**, 181-183 (2006). doi:10.1126/science.1126230

33. A. Gruverman, M. Alexe, D. Meier, Piezoresponse Force Microscopy and Nanoferroic Phenomena. *Nat. Commun.* **10**, 1661 (2019). doi:10.1038/s41467-019-09650-8

34. R. Hinchet, U. Khan, C. Falconi, S.-W. Kim, Piezoelectric Properties in Two-Dimensional Materials: Simulations and Experiments. *Mater. Today* **21**, 611-630 (2018). doi:10.1016/j.mattod.2018.01.031

35. L. Li, M. Wu, Binary Compound Bilayer and Multilayer with Vertical Polarizations: Two-Dimensional Ferroelectrics, Multiferroics, and Nanogenerators. *ACS Nano* **11**, 6382-6388 (2017). doi:10.1021/acsnano.7b02756

References from Supplementary Materials

36. A. Gurarslan *et al.*, Surface-Energy-Assisted Perfect Transfer of Centimeter-Scale Monolayer and Few-Layer MoS_2 Films onto Arbitrary Substrates. *ACS Nano* **8**, 11522-11528 (2014). doi:10.1021/nn5057673

37. P. E. Blöchl, Projector Augmented-Wave Method. *Phys. Rev. B* **50**, 17953-17979 (1994). doi:10.1103/PhysRevB.50.17953

38. G. Kresse, D. Joubert, From Ultrasoft Pseudopotentials to the Projector Augmented-Wave Method. *Phys. Rev. B* **59**, 1758-1775 (1999). doi:10.1103/PhysRevB.59.1758

39. G. Kresse, J. Furthmüller, Efficiency of Ab-Initio Total Energy Calculations for Metals and Semiconductors Using a Plane-Wave Basis Set. *Comput. Mater. Sci.* **6**, 15-50 (1996). doi:10.1016/0927-0256(96)00008-0

40. G. Kresse, J. Furthmüller, Efficient iterative schemes for ab initio total-energy calculations using a plane-wave basis set. *Physical Review B* **54**, 11169-11186 (1996). doi:10.1103/PhysRevB.54.11169

41. M. Dion, H. Rydberg, E. Schröder, D. C. Langreth, B. I. Lundqvist, Van Der Waals Density Functional for General Geometries. *Phys. Rev. Lett.* **92**, 246401 (2004). doi:10.1103/PhysRevLett.92.246401

42. J. Klimeš, D. Bowler, A. Michaelides, Van Der Waals Density Functionals Applied to Solids. *Phys. Rev. B* **83**, 195131 (2011). doi:10.1103/PhysRevB.83.195131

43. J. Qiao, X. Kong, Z.-X. Hu, F. Yang, W. Ji, High-Mobility Transport Anisotropy and Linear Dichroism in Few-Layer Black Phosphorus. *Nat. Commun.* **5**, 4475 (2014). doi:10.1038/ncomms5475

44. J. Hong *et al.*, Exploring Atomic Defects in Molybdenum Disulphide Monolayers. *Nat. Commun.* **6**, 6293 (2015). doi:10.1038/ncomms7293

45. J. Qiao *et al.*, Few-Layer Tellurium: One-Dimensional-Like Layered Elementary Semiconductor With Striking Physical Properties. *Sci. Bull.* **63**, 159-168 (2018). doi:10.1016/j.scib.2018.01.010

46. Z.-X. Hu, X. Kong, J. Qiao, B. Normand, W. Ji, Interlayer Electronic Hybridization Leads to Exceptional Thickness-Dependent Vibrational Properties in Few-Layer Black Phosphorus. *Nanoscale* **8**, 2740-2750 (2016). doi:10.1039/C5NR06293D

47. Y. Zhao *et al.*, Extraordinarily Strong Interlayer Interaction in 2D Layered PtS_2. *Adv. Mater.* **28**, 2399–2407 (2016). doi:10.1002/adma.201504572

48. K.-A. N. Duerloo, M. T. Ong, E. J. Reed, Intrinsic Piezoelectricity in Two-Dimensional Materials. *The Journal of Physical Chemistry Letters* **3**, 2871-2876 (2012). doi:10.1021/jz3012436

49. J. Neugebauer, M. Scheffler, Adsorbate-Substrate and Adsorbate-Adsorbate Interactions of Na and K Adlayers on Al(111). *Phys. Rev. B* **46**, 16067-16080 (1992). doi:10.1103/PhysRevB.46.16067

50. W. Ding *et al.*, Prediction of Intrinsic Two-Dimensional Ferroelectrics in In_2Se_3 and Other III_2-VI_3 Van Der Waals Materials. *Nat. Commun.* **8**, 14956 (2017). doi:10.1038/ncomms14956

51. S. Q. Wang, H. Q. Ye, First-Principles Study on Elastic Properties and Phase Stability of III-V Compounds. *Phys. Status Solidi B* **240**, 45-54 (2003). doi:10.1002/pssb.200301861

52. M. N. Blonsky, H. L. Zhuang, A. K. Singh, R. G. Hennig, Ab Initio Prediction of Piezoelectricity in Two-Dimensional Materials. *ACS Nano* **9**, 9885-9891 (2015). doi:10.1021/acsnano.5b03394

53. R. D. King-Smith, D. Vanderbilt, Theory of Polarization of Crystalline Solids. *Phys. Rev. B* **47**, 1651-1654 (1993). doi:10.1103/PhysRevB.47.1651

54. N. A. Spaldin, A Beginner's Guide to the Modern Theory of Polarization. *J. Solid State Chem.* **195**, 2-10 (2012). doi:10.1016/j.jssc.2012.05.010

55. Z.-Y. Ning, J.-S. Qiao, W. Ji, H. Guo, Correlation of interfacial bonding mechanism and equilibrium conductance of molecular junctions. *Frontiers of Physics* **9**, 780-788 (2014). doi:10.1007/s11467-014-0453-x

56. J. Zhou *et al.*, A Library of Atomically Thin Metal Chalcogenides. *Nature* **556**, 355-359 (2018). doi:10.1038/s41586-018-0008-3

57. A. Ramasubramaniam, Large Excitonic Effects in Monolayers of Molybdenum and Tungsten Dichalcogenides. *Phys. Rev. B* **86**, 115409 (2012). doi:10.1103/PhysRevB.86.115409

58. A. Pierret, H. Tornatzky, J. Maultzsch, Anti-Stokes Photoluminescence of Monolayer WS_2. *Phys. Status Solidi B* **256**, 1900419 (2019). doi:10.1002/pssb.201900419

59. L. J. McGilly *et al.*, Visualization of Moiré Superlattices. *Nat. Nanotechnol.* **15**, 580-584 (2020). doi:10.1038/s41565-020-0708-3

60. L. Wang *et al.*, 2D Piezotronics in Atomically Thin Zinc Oxide Sheets: Interfacing Gating and Channel Width Gating. *Nano Energy* **60**, 724-733 (2019). doi:10.1016/j.nanoen.2019.03.076

61. E. Strelcov *et al.*, Role of Measurement Voltage on Hysteresis Loop Shape in Piezoresponse Force Microscopy. *Appl. Phys. Lett.* **101**, 192902 (2012). doi:10.1063/1.4764939

62. A. Gruverman *et al.*, Tunneling Electroresistance Effect in Ferroelectric Tunnel Junctions at the Nanoscale. *Nano Lett.* **9**, 3539-3543 (2009). doi:10.1021/nl901754t

63. B. Di Bartolo, R. C. Powell, *Crystal Symmetry, Lattice Vibrations and Optical Spectroscopy of Solids*. (World Scientific Publishing Co. Pte. Ltd., Singapore, 2013), pp. 550.

64. G. B. Arfken, H. J. and Weber, F. E. and Harris, *Mathematical Methods for Physicists*. (Elsevier Inc., Waltham (USA), ed. 7, 2013).

65. M. M. Alyörük, Y. Aierken, D. Çakır, F. M. Peeters, C. Sevik, Promising Piezoelectric Performance of Single Layer Transition-Metal Dichalcogenides and Dioxides. *J. Phys. Chem. C* **119**, 23231-23237 (2015). doi:10.1021/acs.jpcc.5b06428

66. W. Wu *et al.*, Piezoelectricity of Single-Atomic-Layer MoS$_2$ for Energy Conversion and Piezotronics. *Nature* **514**, 470-474 (2014). doi:10.1038/nature13792
67. L. Dong, J. Lou, V. B. Shenoy, Large In-Plane and Vertical Piezoelectricity in Janus Transition Metal Dichalchogenides. *ACS Nano* **11**, 8242-8248 (2017). doi:10.1021/acsnano.7b03313
68. J. L. Feldman, Elastic Constants of 2H-MoS$_2$ and 2H-NbSe$_2$ Extracted From Measured Dispersion Curves and Linear Compressibilities. *J. Phys. Chem. Solids* **37**, 1141-1144 (1976). doi:10.1016/0022-3697(76)90143-8
69. H. Peelaers, C. G. Van de Walle, Elastic Constants and Pressure-Induced Effects in MoS$_2$. *J. Phys. Chem. C* **118**, 12073-12076 (2014). doi:10.1021/jp503683h

Corresponding Authors

Shu Ping Lau - Department of Applied Physics, The Hong Kong Polytechnic University, Hong Kong S.A.R., China; orcid.org/0000-0002-5315-8472; E-mail: apsplau@polyu.edu.hk.

Wei Ji - Department of Physics and Beijing Key Laboratory of Optoelectronic Functional Materials & Micro-Nano Devices, Renmin University of China, Beijing 100872, P. R. China; E-mail: wji@ruc.edu.cn

Manish Chhowalla - Department of Materials Science & Metallurgy, University of Cambridge, Cambridge, UK; E-mail: mc209@cam.ac.uk

Supplementary Materials
Materials and Methods

CVD growth. A detailed description of our CVD growth process is provided in SM Section 1. Here, we give a concise overview. The heterobilayers were grown on SiO_2/Si substrates in a quartz tube inside a CVD furnace at atmospheric pressure. We have placed a quartz boat in the center of the heating zone, filled with 30 mg of WO_3 powder and 3 mg of MoO_3 powder, and 10 – 20 mg of KI salt grains. The SiO_2/Si substrates were place upside-down onto this quartz boat to cover the powders. Another quartz boat filled with S powder was placed upstream at the edge of the hot zone. The tube was heated at 50 °C/s to 560 °C in air. Hot air is a powerful cleaning agent and keeps the substrates clean. This air-flow phase is important to keep the MoS_2 growth phase as short as possible. After reaching 560 °C, the air pump is turned off, and H_2/Ar gas mixture (10%) is supplied to the tube for the remainder of the CVD process (Figure S2). The tube is heated to 750 °C and held there for 10 min after which the heater is turned off. Natural cooling to well below 100 °C ends the CVD process.

Transfer. We employed a polystyrene transfer method.(*36*) Detailed step-by-step process description of the method is provided in SM Section 16.

Characterization. Raman and PL measurements were performed using the WITEC confocal Raman system. A green excitation laser (532 nm) was used. Generally, measurements were performed at 1 mW laser power for 1 or 2 seconds. TEM/SAED measurements were carried out with the JEOL JEM2011. Samples are generally transferred onto small copper grids covered with a thin carbon film. AFM, C-AFM and PFM measurements were carried out with the Asylum Research MFP-3D Infinity AFM. Optical microscopy was mostly performed using the LEICA

DMC5400 and LEICA DM2700 M. The cross-sectional STEM samples were fabricated using the FEI Helios 600i dual-beam focused ion beam (FIB) system. The STEM measurements were acquired on a Thermofisher Titan G2 60-300 aberration correction S/TEM microscope with 300 kV acceleration voltage. The FIB and S/TEM were conducted at the National Laboratory of Solid State Microstructures, Jiangsu Key Laboratory of Artificial Functional Materials, College of Engineering and Applied Sciences and Collaborative Innovation Center of Advanced Microstructures, Nanjing University, Nanjing, P. R. China. All other measurements were carried out at the Department of Applied Physics of the Hong Kong Polytechnic University, Hong Kong SAR, P. R. China.
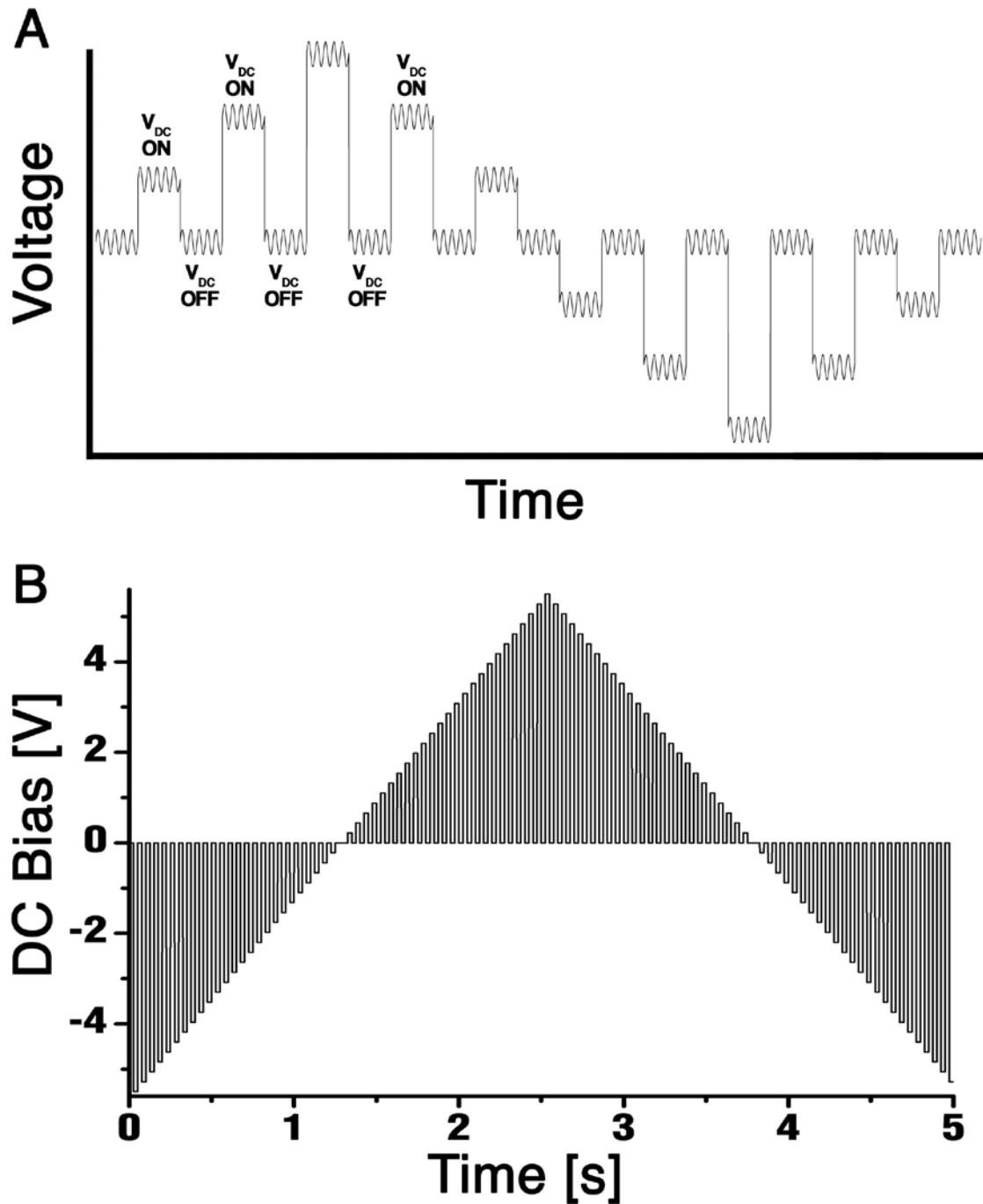
Fig. S1. Voltage-over-time schematic of the DART-SS-PFM spot measurement. (**A**) Conceptual graph of the measurement principle showing both V_{DC} and V_{AC} together. A constant small AC voltage is applied throughout the measurement which functions as the read-voltage. A sequence of DC voltage pulses is applied to the sample (V_{DC} ON). Their amplitudes increase and decrease over time. Each pulse is followed by a short time period (V_{DC} OFF) at which $V_{DC} = 0$. The frequency of V_{AC} used in this conceptual graph is much lower than during an actual measurement and only serves to visualize the principle. (**B**) The actual DC voltage programme used to measure

the data from Figure 3(A, B). The duration of each single pulse was 0.025 s. The simultaneous AC voltage had a frequency of ~ 350 kHz.

PFM measurement principle. DART-SS-PFM mode was used for PFM maps to ensure strong signal-to-noise ratio.(*19*) DART stands for "Dual Amplitude Resonance Tracking", the SS stands for "Switching Spectroscopy". In PFM, a cantilever with a conductive AFM tip is brought in close proximity to the vertical heterostructure surface, and contact mode mapping is performed in the presence of an oscillating electric potential $V = V_{\text{DC}} + V_{\text{AC}}\cos(\omega t)$. A piezoelectric material responds to the applied voltage by stretching or contracting. The piezoelectric constant tensor components can then be extracted – including the one for OOP, d_{33}. This component is the ratio between the vertical deformation magnitude Δz and the electric potential V applied in the OOP direction. Thus, the vertical deformation magnitude can be calculated by $\Delta z = d_{33}V = d_{33}V_{\text{DC}} + d_{33}V_{\text{AC}}\cos(\omega t + \varphi)$. The phase shift φ is included to account for the polarization directions of the crystal lattice. For instance, if two neighboring regions are polarized in exactly the opposite directions, the difference in phase shift $\Delta\varphi$ will be 180°. The signal-to-noise ratio in regular PFM maps can be small which demands careful analysis for key parameters to be extracted. However, each PFM cantilever has a resonance frequency, ω_0, that primarily depends on the cantilever material and tip morphology as well as slightly on the contact surface morphology. When measuring close to the resonance frequency, the PFM setup will not detect Δz directly but instead a much stronger amplitude *A,* which is defined as $A = d_{33}V_{\text{AC}}Q$. That is, the vertical deformation multiplied by the quality factor Q. Mapping this amplitude provides a much clearer picture of PFM data and their maps because it has a large signal-to-noise ratio. Then, for analytical purposes, $\overline{\Delta z}$, Q and φ can be extracted from the amplitude measurements, where $\overline{\Delta z}$ is the maximum vertical deformation at any given voltage (i.e. whenever $\cos(\omega t + \varphi) = 1$). For regular PFM mapping V_{DC} is generally set to zero as it does not add any information to the measurement of a piezoelectric

surface. However, when performing SS-PFM, a V_{DC} voltage sweep is performed while $V_{AC} \cos(\omega t + \varphi)$ is also active. As shown in Figure S1, the V_{DC} sweep in DART-SS-PFM is a consecutive on-and-off switching of V_{DC} while its magnitude slowly increases and decreases for multiple cycles. While V_{DC} is switched on, a ferroelectric surface can be poled in the direction of the electric field. During both on- and off-periods, the piezoresponse is measured, such that the ON-field and OFF-field piezoresponse hysteresis loops of the material can be plotted. The use of plotting both ON- and OFF-field loops is to differentiate between simply piezoelectric and combined piezoelectric/electrostrictive deformations.

The LithoPFM mode of the Asylum Research software is used for permanent domain writing of a ferroelectric surface. Here, the PFM tip carries a strong constant DC voltage while being moved in contact mode across the surface. The electric field will then reorient ferroelectric domains under the tip in accordance with the electric field direction. By changing V_{DC} at different locations, any predetermined 2D pattern can be imprinted into a ferroelectric surface, such that the material gains distinct regions with uniform polarization directions. This pattern can then be read using PFM mapping and will be visible in the amplitude and phase maps.

DFT calculations. Our DFT calculations were performed using the generalized gradient approximation (GGA) for the exchange-correlation potential, the projector augmented-wave (PAW) method(*37, 38*) and a plane-wave basis set as implemented in the Vienna ab-initio simulation package (VASP)(*39, 40*). Dispersion correction was made at the van der Waals density functional (vdW-DF) level(*41, 42*), using the optB86b functional for the exchange potential, which was proven to be accurate in describing the structural properties of the layered materials(*43-47*) and was adopted for structure-related and electric polarization calculations. A $\sqrt{3} \times 1$

orthorhombic supercell(*48*) consisting of an MoS$_2$ and a WS$_2$ monolayers were used to model the hetero-bilayer, in which the armchair and zig-zag directions were denoted with x and y, respectively. A 20 Å vacuum layer was used to reduce interactions among adjacent image layers. The kinetic energy cut-off for the plane-wave basis set was set to 500 eV for geometric relaxations and electric polarization calculations. A *k*-mesh of 9×15×1 was adopted to sample the first Brillouin zone of the $\sqrt{3} \times 1$ supercell. In structural relaxations, all ionic positions and the shape and volume of the supercell were allowed to relax until the residual force on each atom was less than 0.005 eV/Å. A dipole correction along the *z*-direction is considered in all calculations to correct the artificial electric polarization introduced by the periodic boundary condition and to balance the vacuum level differences on the different sides of the MoS$_2$/WS$_2$ bilayers.(*49, 50*)

Derivation of piezoelectric constant tensors. The piezoelectric strain constant tensor *d*, which was directly measured in our experiments, is defined by relation $d = eC^{-1}$. We calculated the elastic constant tensor *C*, including both electronic and ionic contributions, by fitting the energy-strain curve(*51*) with a series of strain values applied from -0.01 to 0.01 in a step of 0.005 in a certain direction. The piezoelectric constant tensor elements e_{ij} are calculated by equation $e_{ij} = \partial P_i / \partial S_j = e_{ij}^{elc} + e_{ij}^{ion}$, where *i, j, k* ∈ (1, 2, 3) represent the directions *x*, *y* and *z*. This equation represents a uniform strain *S* applied to the *j* direction which induces an electric polarization change ΔP along the *i* direction.(*52*) In the following decomposed form, the former term, known as clamp-ion term, results from the electronic contribution, which was calculated with fixed atomic positions under strain. The latter term arises from the internal relaxation of ions under strain. Because of the 20 Å vacuum layer in the *z*-direction, we have to fix the *z*-coordinates of the top and bottom atomic layers to efficiently apply strains in *z* to calculate all *z*-relevant components,

i.e. C_{33}, C_{13}, e_{33} and e_{31}. The electric polarization change ΔP is calculated using the Berry phase method, defined as $\Delta P = \Delta P_{ion} + \Delta P_e$, where ΔP_{ion} and ΔP_e refer to the ionic and electronic contributions, respectively, as implemented in VASP.(*53, 54*)

Modelling for ferroelectric tunnel junctions. A dual-slab model, usually adopted for molecular transport junctions(*55*), was used in modelling the FTJ formed in the experiments. The model contains a $\sqrt{3} \times \sqrt{3}$ MoS_2/WS_2 bilayer, sandwiched by two four-layer-thick 2×2 Pt (111) slabs, and separated by a vacuum layer of over 20 Å. The lattice constant of Pt was optimized 2.797 Å and 3.167 Å for MoS_2/WS_2, which leads to a reasonable lattice mismatch of 1.9%. While the originally used optB86b-vdW function is less efficient for such large volume supercell, we used the PBE-D3 functional, which shows a highly comparable performance with the optB86b-vdW functional, for all dual-slab model calculations. The kinetic energy cut-off for the plane-wave basis set was set to be 450 eV. A *k*-mesh of 11×11×1 was adopted to sample the first Brillouin zone. In structural relaxations, positions of all atoms were allowed to fully relax until the residual force on each atom was less than 0.01 eV/Å, except for the top and bottom two layers of the Pt slabs, whose positions were kept fixed in their bulk positions. In band structures calculations, either the Γ-K or Γ-M path was equally sampled using 21 *k*-points in the reciprocal space.

Supplementary Text
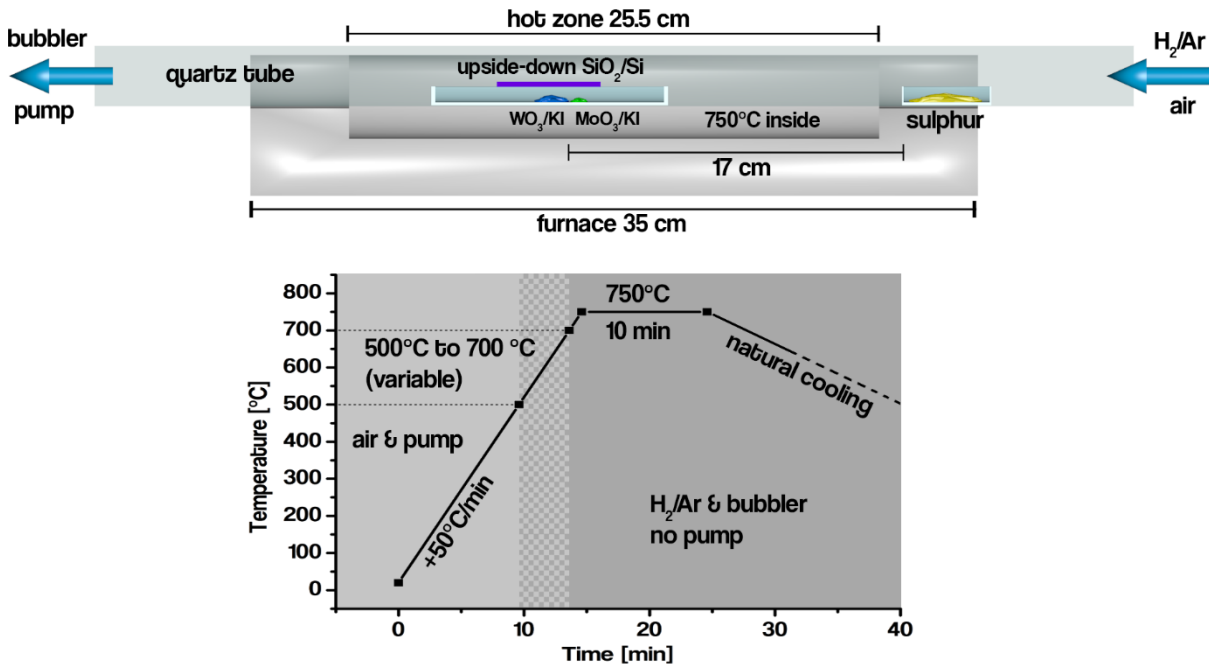
Section 1: CVD growth recipe in detail.

Fig. S1. Schematic of setup and growth temperature overview for one-step CVD growth of the MoS$_2$/WS$_2$ heterobilayers on SiO$_2$. The top schematic shows the arrangement of powders, quartz boats and the substrate for the CVD process, as well as the physical dimensions of the furnace. The graph shows the temperature development in the tube center over time. In the heating phase of the process, the gas in the tube is switched from pumped air (marked in light grey) to H$_2$/Ar gas mix (dark grey).

The growth is done at atmospheric pressure. SiO$_2$ (525 nm) on Si substrates are placed face-down on top of a quartz boat in the middle of a single CVD heating zone inside a 1-inch diameter quartz tube. The process also works on 300 nm SiO$_2$. The wafer is pre-cleaned with acetone, IPA and DI water and then treated with O$_2$-plasma for a few minutes. The quartz boat is filled with 30 mg of WO$_3$ powder and 3 mg of MoO$_3$ powder. In addition, we sprinkle between 10 – 20 mg of potassium iodide (KI) on top of these powders as described by Zhou *et al.*(*56*) Their recipe includes NaCl and KI as growth seeds that yield good results. We use KI instead of NaCl for the growth

process because after trying both salts, KI yielded better results. To convert the mass of NaCl to KI, while keeping the molar amount constant, the formula: $m_{KI} = 2.84 \cdot m_{NaCl}$ was used. An additional quartz boat filled with sulfur powder was placed upstream of the furnace. For an overview of the correct placement of all ingredients as well as the growth instructions, refer to Figure S1. For the initial growth phase, air is pumped through the tube to make sure that all gas in the quartz tube moves downstream at any time. This phase of pumping in the air instead of hydrogen during the initial heating period is important to keep the effective growth time for MoS_2 as short as possible, relative to the WS_2 growth time. Otherwise, the substrate is covered with a thick layer of bulky MoS_2 crystals. The hot air in the tube keeps the growth substrate clean, initially. The tube is heated at a rate of 50 °C/s in pumped air, until the inside temperature reaches 500-700 °C. At that point, the pump is turned off and the H_2/Ar inlet valve is opened. The gas now exits the tube through a bubbler. The choice of the temperature for switching gases dictates the growth outcome. Lower the switching temperature leads to sharper edges of the triangles but also smaller triangle dimensions. Higher switching temperature leads to larger but more irregularly shaped heterostructures and eventually to additional layers. In Figure S2 we showcase optical microscopy images of the growth results depending on the switching temperature, ranging from 500 °C to 700 °C. For our experiments on SHG and PFM we used 560 °C as the switching point. The H_2/Ar gas flow is set to 100 sccm. As the temperature in the furnace rises so does the temperature around the sulfur boat, thereby slowly evaporating more and more sulfur powder, creating a continuous flow of sulfur vapor. The furnace is heate upto 750 °C and held for 10 min after which the heating is switched off and the tube cools down naturally to < 100 °C.

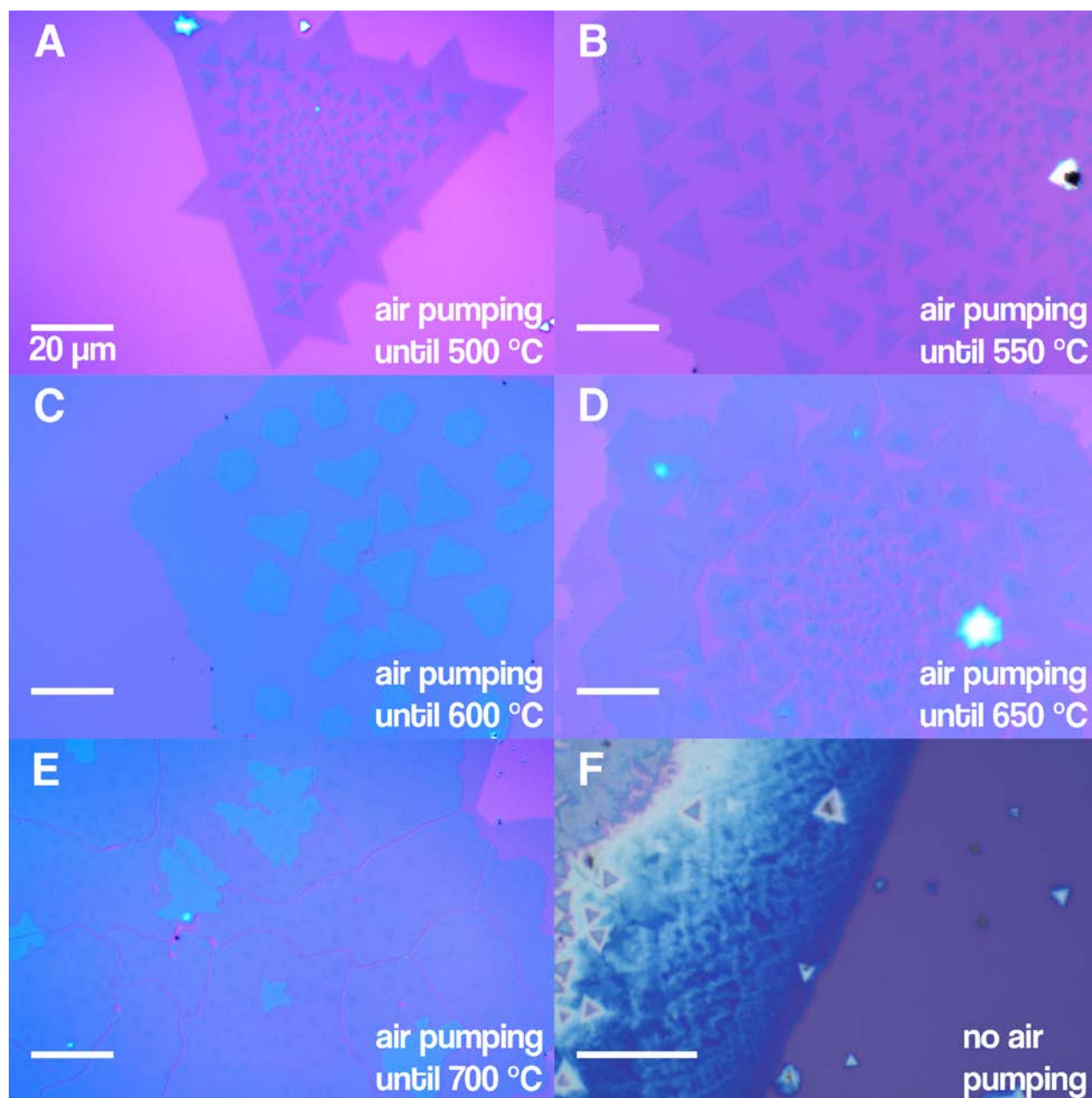*Section 2: Controlling growth shapes through temperature.*

Fig. S2. Optical images of the CVD results depending on the temperature at which the furnace atmosphere is switched from pumped air to Ar/H_2.

As mentioned before, the size and shape of the heterostructures produced by CVD can be controlled via the choice of temperature when the pumped air is shut off from the quartz tube, and H_2/Ar gas mix is let into the tube. We present a number of optical images in Figure S3 that showcase the shape and size evolution depending on the switching temperature. The triangles are the smallest and sharpest when the switch occurs at 500 °C (Figure S2(A)). The large monolayer MoS_2 clusters also have very sharp edges. At 550 °C the triangles get larger, and the MoS_2 cluster edges become less sharp and show some large particles around the edges. At 600 °C the triangles lose their sharp edges and do not look like triangles anymore. The MoS_2 cluster has round edges. At 650 °C and above the WS_2 areas increase in size until they merge to form an entire layer below the MoS_2 cluster. Additional layers start forming. The ideal process, however, is not to omit phase 1 entirely, as shown in Figure S2(F). Without vacuum pumping, the CVD process grows large, thick, bulk material clusters with a very irregular pattern.

Section 3: Bright Field cross-sectional STEM.
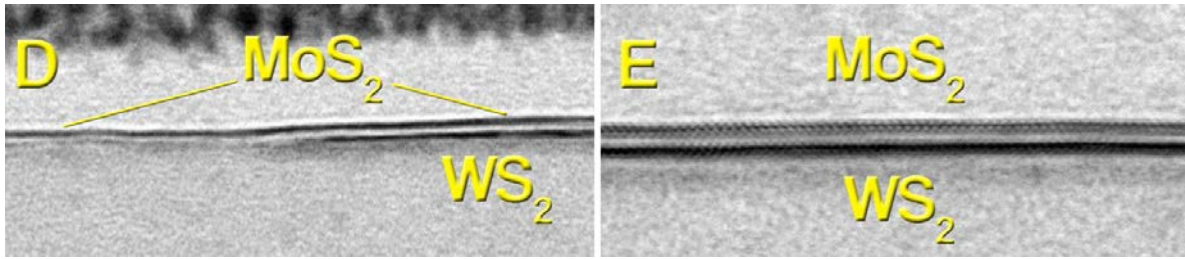

Fig. S4. BF-STEM images corresponding with the HAADF-STEM images from Figure 1.

In Figure S4, we show the Bright Field STEM images of the cross-sectional STEM analysis. The labels d and e are in reference to the locations indicated in Figure 1(C). They tell the same story as the HAADF-STEM images. Here, the brighter lines are MoS_2 layers, and the darker lines are WS_2 layers.

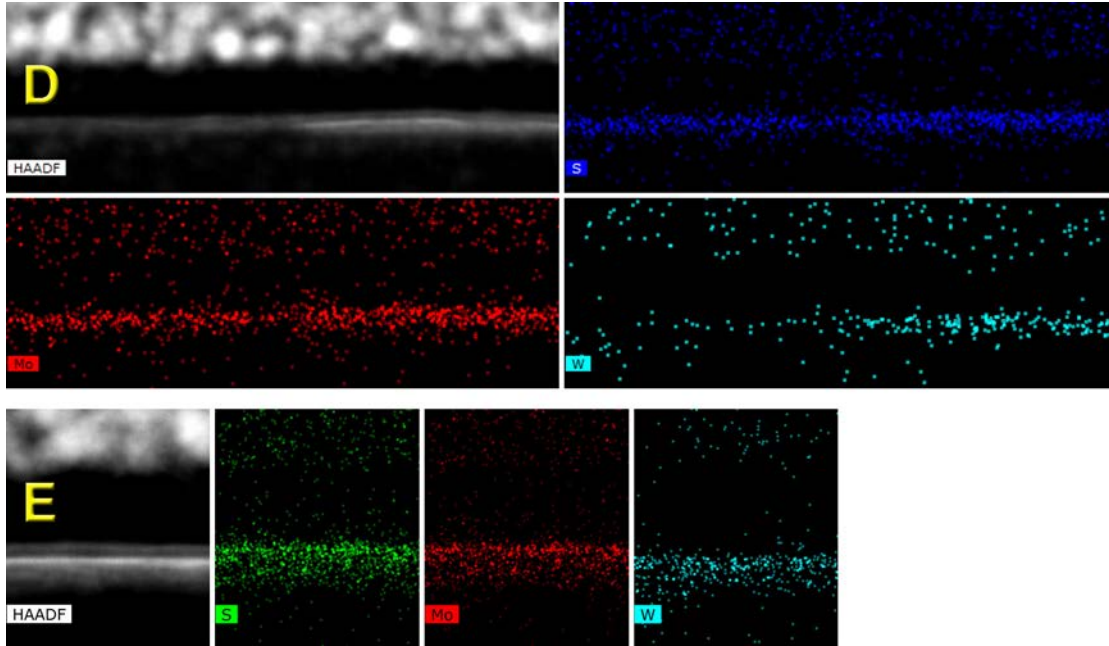*Section 4: EDS mappings of cross-sectional STEM.*

Fig. S5. EDS analysis of the cross-section STEM measurements from Figure 1. The labels (**D)** and (**E**) are in reference to the locations indicated in Figure 1(C). For each location, the HAADF-STEM image, as well as the EDS mappings for S, Mo and W atoms are shown.

While performing the cross-sectional STEM, we have also recorded the EDS mappings of each location to properly identify the material in each layer. We also need to take into consideration what we know from Raman mapping to come to our conclusions. At the triangle edge from Figure S5(D) we find Mo and S atoms across the entire length of the image, but W atoms are only found on the right side beneath the Mo atoms, indicating that the large monolayer clusters are purely MoS_2, whereas the triangle area is WS_2 covered by MoS_2. Figure S5(E) shows an even distribution from left to right of Mo atoms on top and W atoms below, and S atoms in both layers, revealing that we have a heterostructure of MoS_2/WS_2.

37

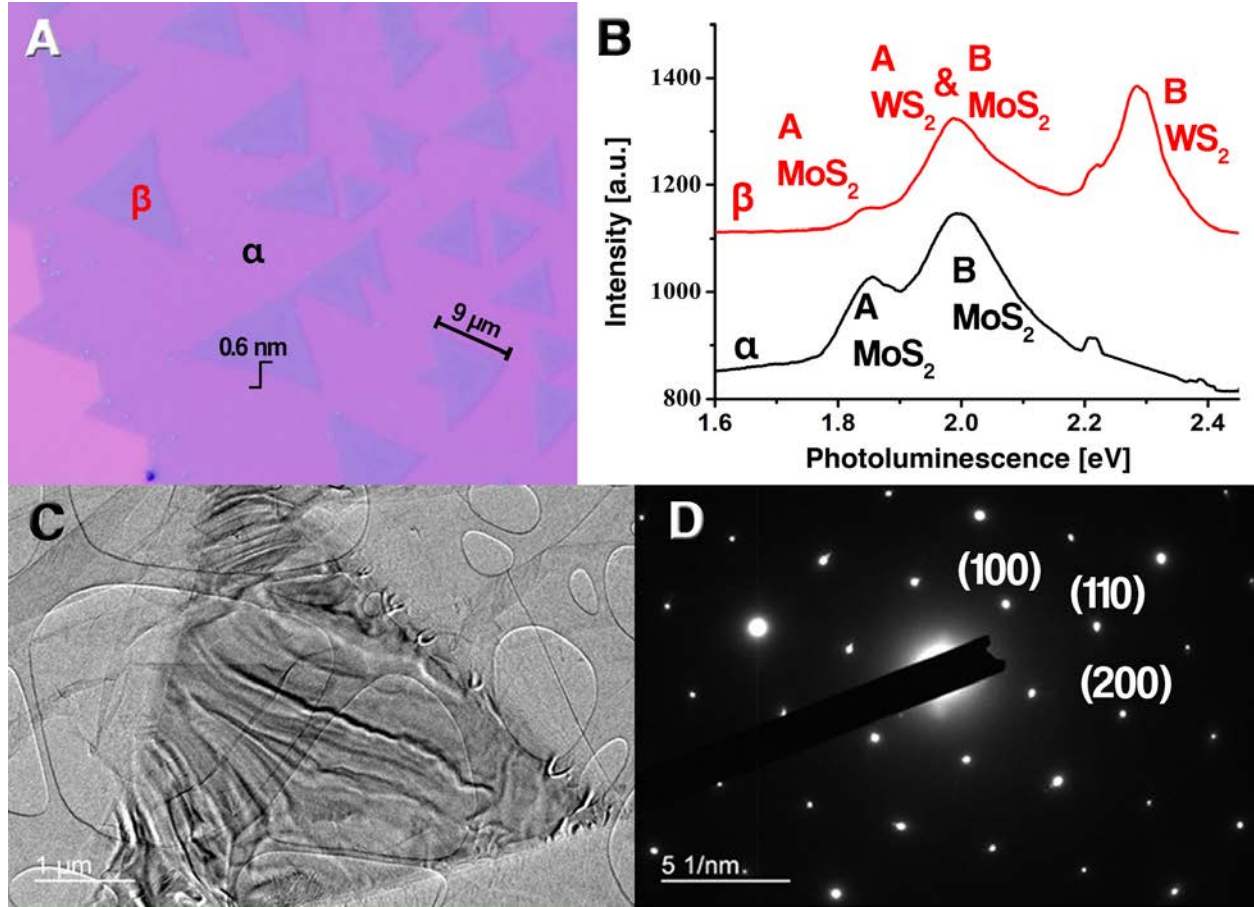*Section 5: Photoluminescence and SAED spectra.*

Fig. S6. Further material characterization. (**A**) The optical microscope image from Figure 1(A), for easier reference. (**B**) The corresponding PL spectra of the locations α and β. α shows only the A- and B-peak of MoS_2; β shows the A- and B-peaks of both MoS_2 and WS_2, however the B-peak of MoS_2 and the A-peak of WS_2 overlap. (**C**) TEM image of a typical MoS_2/WS_2 triangle. (**D**) Corresponding SAED spectrum of the triangle in (C). The spectrum shows two completely overlapping single crystal patterns.

We also examined the PL spectra of the sample, shown in Figure S6(B). The pure monolayer MoS_2 has an A-peak at 1.84 eV (673 nm) and a stronger B-peak at 2.0 eV (619 nm).(*57*) When measuring the MoS_2/WS_2 triangles, we find both A-peak and B-peak of WS_2 at 2.01 eV (616 nm) and at 2.28 eV (543 nm), respectively,(*58*) as well as the PL emission of MoS_2. The A-peak of MoS_2 is visible, however strongly quenched. The B-peak is likely also strongly quenched, and since the B-peak of

MoS$_2$ and the A-peak of WS$_2$ are very closely located, we can only measure them together as one broad peak at around 2.0 eV.

Figure S6(C) shows the TEM image of a MoS$_2$/WS$_2$ heterobilayer triangle, transferred onto a copper grid covered with a thin carbon film that is somewhat visible through the round shapes all across the image, since the carbon film has many holes. The corresponding SAED pattern of is shown in Figure S6(D). The pattern shows only discrete dots and not bright rings, indicating that the measured crystal is a single crystal domain. Looking closely, it becomes apparent that the pattern is actually two patterns that almost completely overlap. These two patterns are from the MoS$_2$ layer and the WS$_2$ layer. Both materials have identical lattice vectors, which is why their SAED patterns can overlap. The overlapping also indicates that both layers are fittingly oriented, rather than randomly. This is in agreement with our SHG analysis.

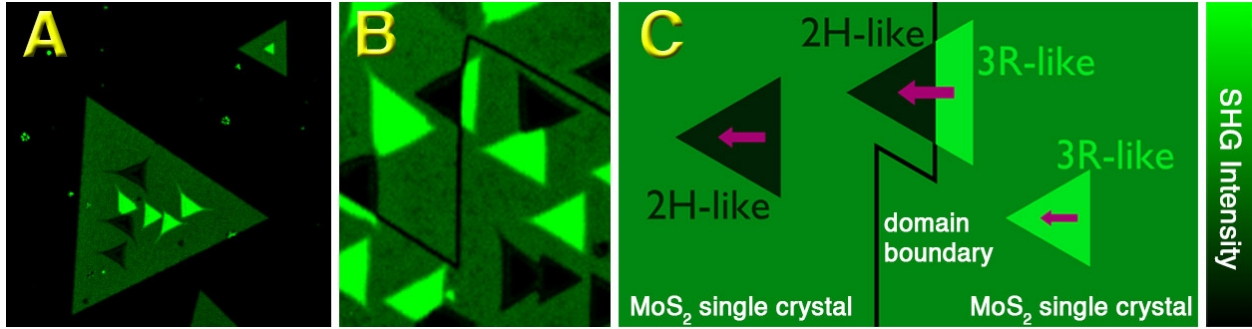*Section 6: SHG analysis of the heterobilayer geometry.*

Fig. S7. SHG geometry analysis. (**A**) SHG map of two large triangular single crystals of MoS_2 draped over several smaller WS_2 triangles. No domain boundaries are present. (**B**) SHG map of a large MoS_2 area with a domain boundary passing through it. Some WS_2 triangles are located under that domain boundary. The schematic classification of the observations in (A, B) is displayed in (**C**). Domain boundaries flip bright and dark triangle directions, indicating that different MoS_2 domains have opposite orientations.

Our SHG maps in Figure S7 reveal many details about the heterobilayers. Figure S7(A) shows two large MoS_2 single crystals in triangular shape. They are oriented oppositely from each other: the smaller MoS_2 layer on the top right is pointing left, the larger MoS_2 layer on the bottom left is pointing right. The MoS_2/WS_2 triangles' SHG emission is either very intense (bright green) or very dim (almost black), depending on their orientation relative to the MoS_2 cover, due to SHG interference between the layers.(*14*) Those triangles with the same orientation as the MoS_2 cover appear very bright; those with the opposite orientation appear very dark. This is in agreement with our observations from our STEM measurements shown in SM Section 7. The single crystal domain boundaries of the large MoS_2 layer have become visible in the SHG map as thin black lines (see Figure S7(B)). Bright triangles always point toward the closest domain boundaries; dark triangles always point away from them. We know that the dark bilayer triangles are dark because their inter-layer angle $\theta = 180°$. This is the same type of stacking as bilayer 2H MoS_2, and thus we label the dark triangles as 2H-like. Conversely, the bright triangles have $\theta = 0°$ which resembles the

structure of bilayer 3R MoS$_2$, and thus we call the bright triangles 3R-like. In Figures S7(B, C) we focus on a domain boundary of the large MoS$_2$ layer. The boundary passes over one triangle, which causes the triangle's SHG signal to be very bright on one side of the boundary and very dark on the other side. The MoS$_2$/WS$_2$ triangle is partially 3R-like and partially 2H-like. This means that there is also a rotation angle of 180° between neighboring monolayer MoS$_2$ single crystal domains. It also indicates that our monolayer MoS$_2$ domain boundaries form along zig-zag edges.
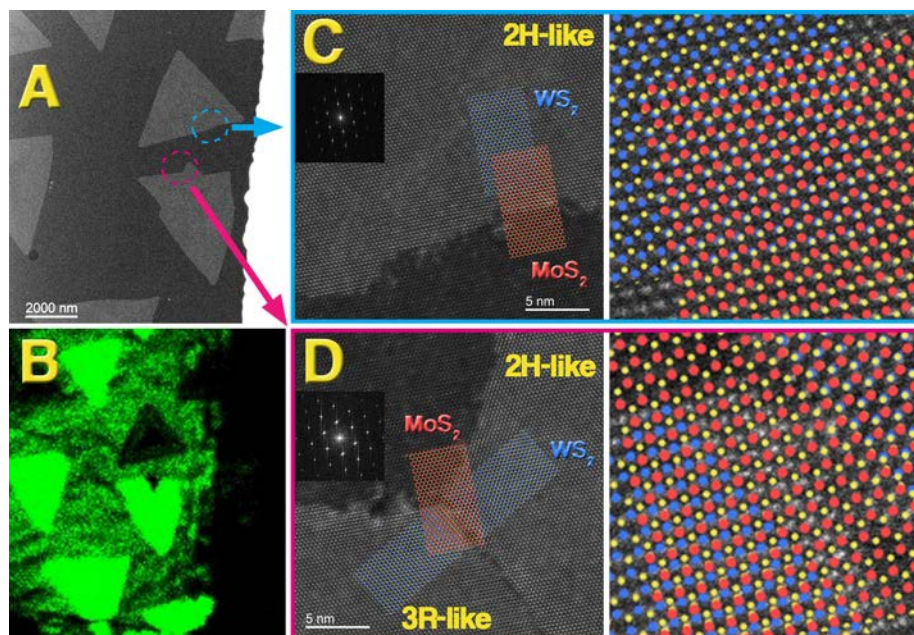
Section 7: STEM stacking analysis of SHG types.

Fig. S8. STEM geometry analysis of the heterobilayer triangles. (**A**) SEM image of two triangles used for top-down HAADF-STEM. The triangles look similar apart from their orientation. The blue and magenta circles indicate where the STEM images were taken from. (**B**) SHG map of the triangles. The dark SHG emission of the top triangle indicates 2H-like stacking, the bottom triangle is mostly very bright and therefore 3R-like but it has a dark corner at the top which is 2H-like. This means that triangle is really two opposite triangles fused together. (**C, D**) HAADF-STEM images of the edges of the 2H-like (C) and 3R-like (D) triangle. Heterobilayer areas appear especially bright due to the heavy tungsten atoms. We can see the domain boundary between the large 3R-like and small 2H-like parts of the bottom triangle. The insets show the Fast Fourier Transform (FFT) of the respective STEM images. In each STEM image a model for MoS_2 and WS_2 monolayers have been overlaid, where Mo atoms are red, W atoms are blue and S atom pairs are yellow. The area where these models intersect (enlarged pictures on the right side) reveals the stacking types.

The correlation between the layer stacking and SHG intensities is confirmed via top-down HAADF-STEM imaging, the results of which are shown in Figure S8. The SEM image in Figure S8(A) shows two triangles selected for analysis. Their SHG map in Figure S8(B) shows that the upper triangle is a 2H-like and the lower triangle a 3R-like heterobilayer. Note that the lower triangle has a small 2H-like corner attached to it (appears dark in SHG). Two bilayer triangles grew together here, however, the 3R-like triangle is significantly larger. Figures S8(C, D) are the

HAADF-STEM images of the triangle edges as indicated in the SEM image. The STEM image in (D) was taken at the intersection between the 3R-like triangle and its small 2H-like add-on. Both STEM images show that our material is highly crystalline, which is confirmed by the FFT maps in the insets showing discrete diffraction dots. Both carry a regular hexagonal pattern that is indistinguishable from that of pure MoS_2 or WS_2 single crystals due to the epitaxial growth of the bilayers. We have overlaid crystal models of MoS_2 and WS_2 monolayers onto each HAADF-STEM image, according to the real atom locations. In the areas where they intersect, the stacking type of each triangle can be clearly distinguished (as detailed in Figure 4), which matches the classification from SHG. A quick rule of thumb: in 2H-like stacking, the W atoms are covered by the S atom pairs of MoS_2, whereas that is not the case for 3R-like stacking.
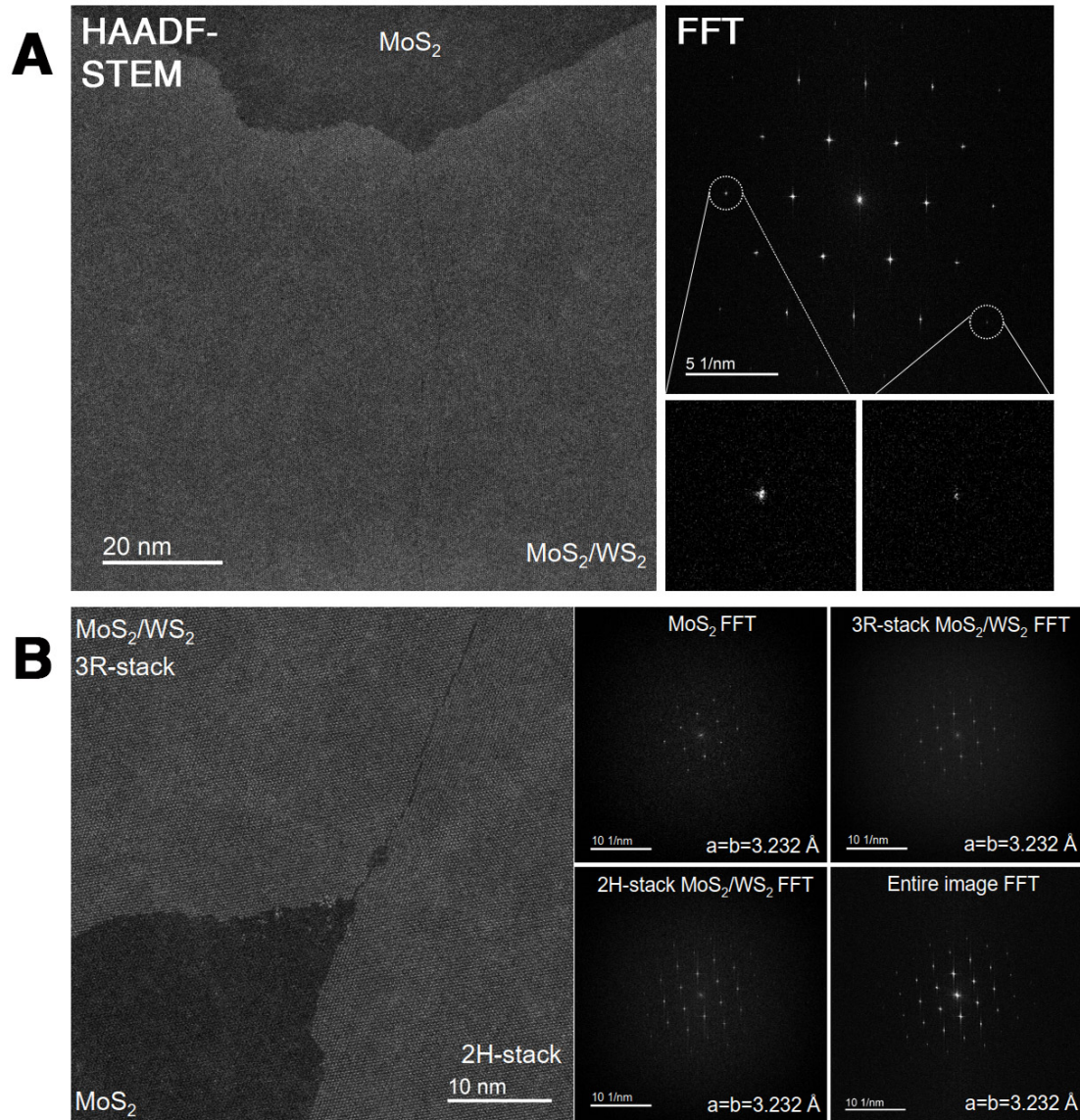
Section 8: Considerations on Moiré patterns.

Fig. S9. Further STEM image analysis of the MoS_2/WS_2 heterobilayer. (**A**) Large scale HAADF-STEM image near the edge of two grown-together heterobilayer triangles with equal orientation. The corresponding FFT spectrum of the entire image is shown on the right side. No pattern splitting can be observed from any of the FFT spots. (**B**) HAADF-STEM image near the edge of two grown-together heterobilayer triangles with opposite orientation. Corresponding FFT spectra for the entire image, as well as the separate 3R-like, 2H-like and pure MoS_2 areas are shown on the right.

Recently, papers showing piezo- and ferroelectricity in twisted bilayers of hBN and TMDCs have been published.(*8, 9, 11, 59*) In these works single- or few-layers of TMDCs or hBN are manually

exfoliated and transferred onto each other at very small twist angles (~ 0.1°). The twist angles being non-zero is essential here, as it gives rise to the occurrence of Moiré patterns even in two layers that share the same lattice parameters. The observed condensed matter phenomena were explained as a consequence of the Moiré superlattice.

To demonstrate the absence of Moiré patterns in our heterobilayers, we provide detailed STEM data. In Figure S9(A) we show a wide area view of the edge of our heterobilayer. At this scale the edges of Moiré patterns would become apparent for artificially stacked bilayers with small stacking angles. However, this is not the case here. The fine dark vertical line in the centre of the heterobilayer is a domain boundary. The STEM image shows the edge of two heterobilayer triangles of the same orientation that grew together. The corresponding FFT spectrum of the image shows a single hexagonal crystal pattern, just like the SAED pattern from Figure S6(D), even though we know that there are both MoS_2 and WS_2 present, which indicates that both layers are commensurate due to the epitaxial growth and their twist-angle is indeed a clean *n·60°*. Figure S9(B) shows the STEM image of another location where a 3R-like and 2H-like triangle grew together. The domain boundary is much more prominent. However, here too is no sight of any Moiré patterns. We have added the FFT spectra for the entire image, as well as just the MoS_2, the 3R-like heterobilayer and the 2H-like heterobilayer area for comparison. All four tell the same story of matching layer stacking. From the realisation of epitaxially matched stacking we have constructed our mathematical model of the heterobilayer which we elaborate on in the Group Theory and DFT sections.

Section 9: PFM map analysis method.

To account for unexpected external influences during PFM measurements, such as tip degradation, scan direction, spontaneous surface charges or surface/crystal irregularities, we employed a statistical analysis method for our data.(*60*) We have performed PFM mapping for several different 2H-like and 3R-like triangles. The ibw-files from the Asylum Research software were converted into csv-files. We then took a large amount of data points of either MoS_2/WS_2 or pure MoS_2, separately, and plotted out the $\overline{\Delta z}$ distributions are shown in Figure 2(C). These distributions represent the full extent of how much the driving voltage deforms the material surface. We then extracted the average value of each distribution to represent that particular measurement. To account for offsets from the software/hardware we took the $\overline{\Delta z}$ distribution averages of MoS_2 as reference point because 1H MoS_2 is known to be non-piezoelectric in the OOP direction. The evolution of these distribution averages from many different measurements was then plotted versus the driving voltage, as shown in Figure 2(D). The linear fit of this plot then gave us the piezoelectric constant d_{33} for both triangle types.
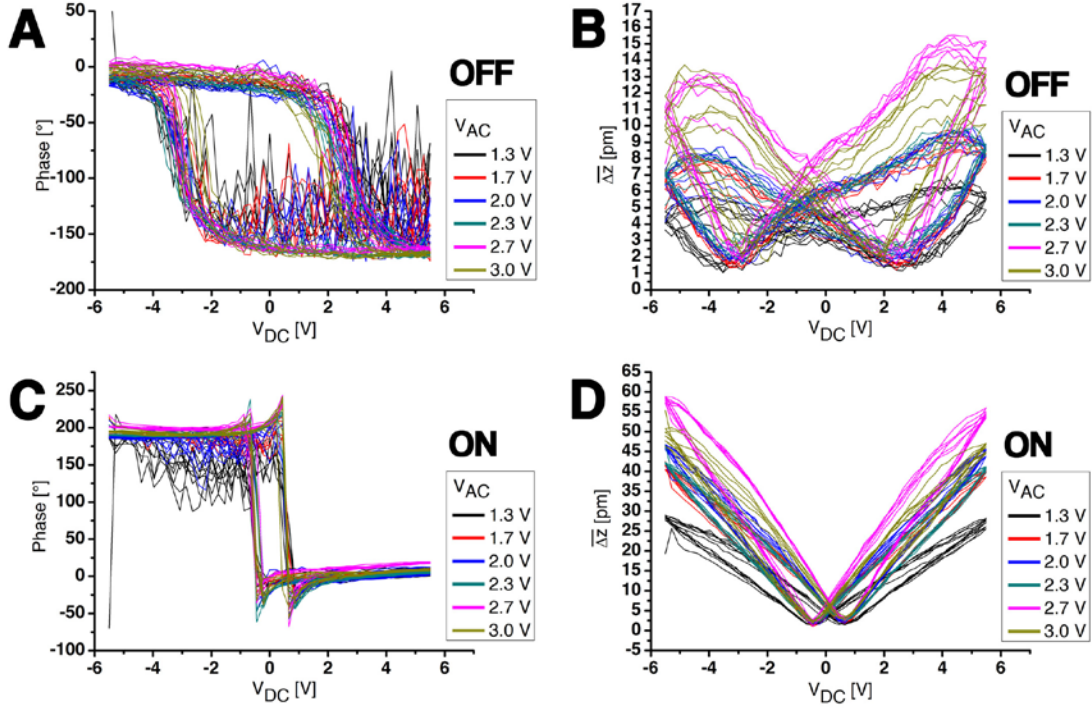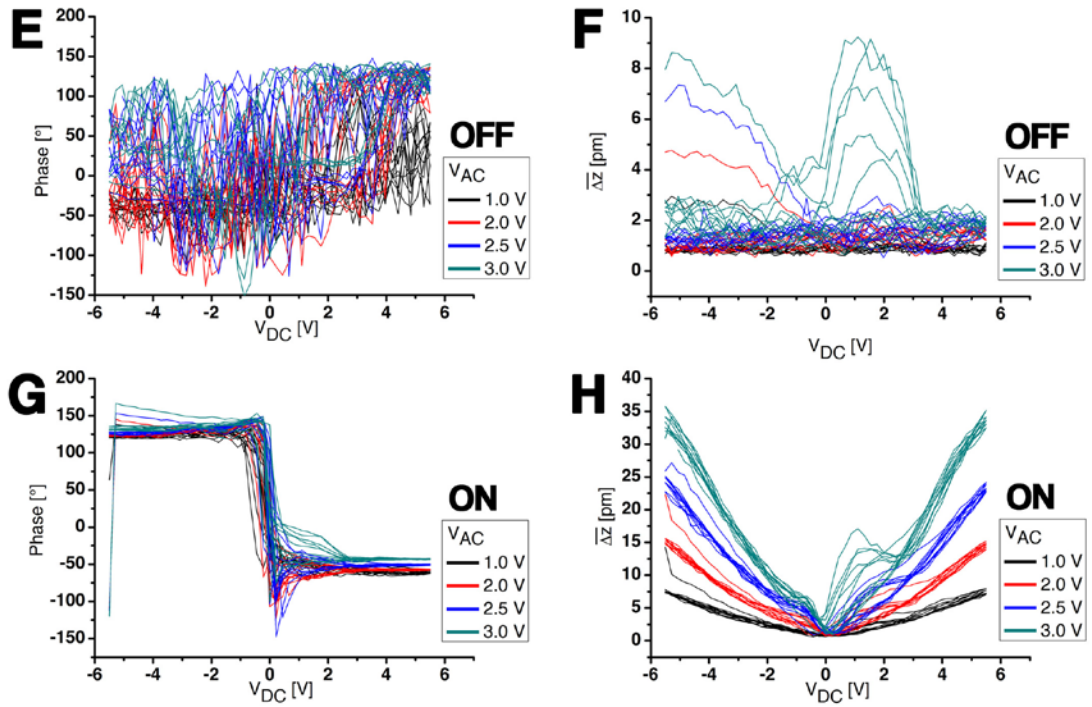
MoS₂/WS₂

MoS₂

Fig. S10. Piezoresponse hysteresis loops of MoS$_2$/WS$_2$ heterobilayer (**A-D**) and simple monolayer MoS$_2$ (**E-H**) at various AC driving voltage as indicated. (A, E) Off-field phase hysteresis loops. (B, F) Off-field $\overline{\Delta z}$ hysteresis loops. (C, G) On-field phase hysteresis loops. (D, H) On-field $\overline{\Delta z}$ hysteresis loops.

A way to distinguish ferroelectric and non-ferroelectric piezoresponse loops is by performing the SS-PFM repeatedly with different values for the driving voltage V_{AC}.(*61*) We can see in Figure S10(B) the butterfly loop increasing in volume, up to the point where V_{AC} exceeds 2.7 V. At 3.0 V the loop shrinks again. We can observe this in both the off- and on-field loops as should be expected. This is explained by V_{AC} reaching the domain switching voltage. At this point, the repeatedly-direction-switching V_{AC} and the unidirectional V_{DC} come in conflict and the domain switching of the material is controlled to some degree by both voltages. This loop breakdown isn't observed for non-ferroelectric piezoelectrics. Hence we find that the MoS$_2$/WS$_2$ triangle does indeed show ferroelectric properties. The same breakdown behavior is also observable in the on-field butterfly loop in Figure S10(D). Both off-field and on-field phase loops shown in Figures S10(A, C), respectively, do not show any significant changes in response to the increase of the driving voltage.

To contrast our findings regarding the ferroelectric character of our MoS$_2$/WS$_2$ heterobilayer, we have also performed the exact piezoresponse hysteresis measurements on the pure monolayer MoS$_2$ areas that surround the triangles. As the off-field phase graph in Figure S10(E) reveals, no consistent ferroelectric phase loop shape was found. Instead, the measured phase appears random and different for every cycle, showing that there is no reliable vertical polarization present but possible spontaneous surface charges that come from the PFM tip. The variation of the AC driving voltage does not introduce any changes. Figure S10(F) shows the corresponding off-field $\overline{\Delta z}$ hysteresis graph. Again no actual loop or butterfly shape is apparent. Rather we see a mostly flat series of graphs. The $\overline{\Delta z}$ magnitude increases slightly with both V_{AC} and V_{DC}, which

hints at small non-ferroelectric interactions with the PFM tip. The on-field phase hysteresis graph in Figure S10(G) also shows no ferroelectric loop shape. Instead, we see an abrupt phase jump around $V_{DC} = 0$ V, independent of the value for V_{AC}. The on-field $\overline{\Delta z}$ hysteresis graph in Figure S10(H) shows the typical V-shape that is caused by the strong unipolar DC-field via electrostriction. At the base of the V-shape no ferroelectric butterfly shape is apparent. Note also that the Δz magnitude does not collapse when the AC driving voltage reaches 3.0 V as it does for MoS_2/WS_2. Thus, the measured piezoresponse hysteresis loops fit the non-ferroelectric character of monolayer 1H MoS_2 and stand in contrast to the measured loops for our heterobilayer.

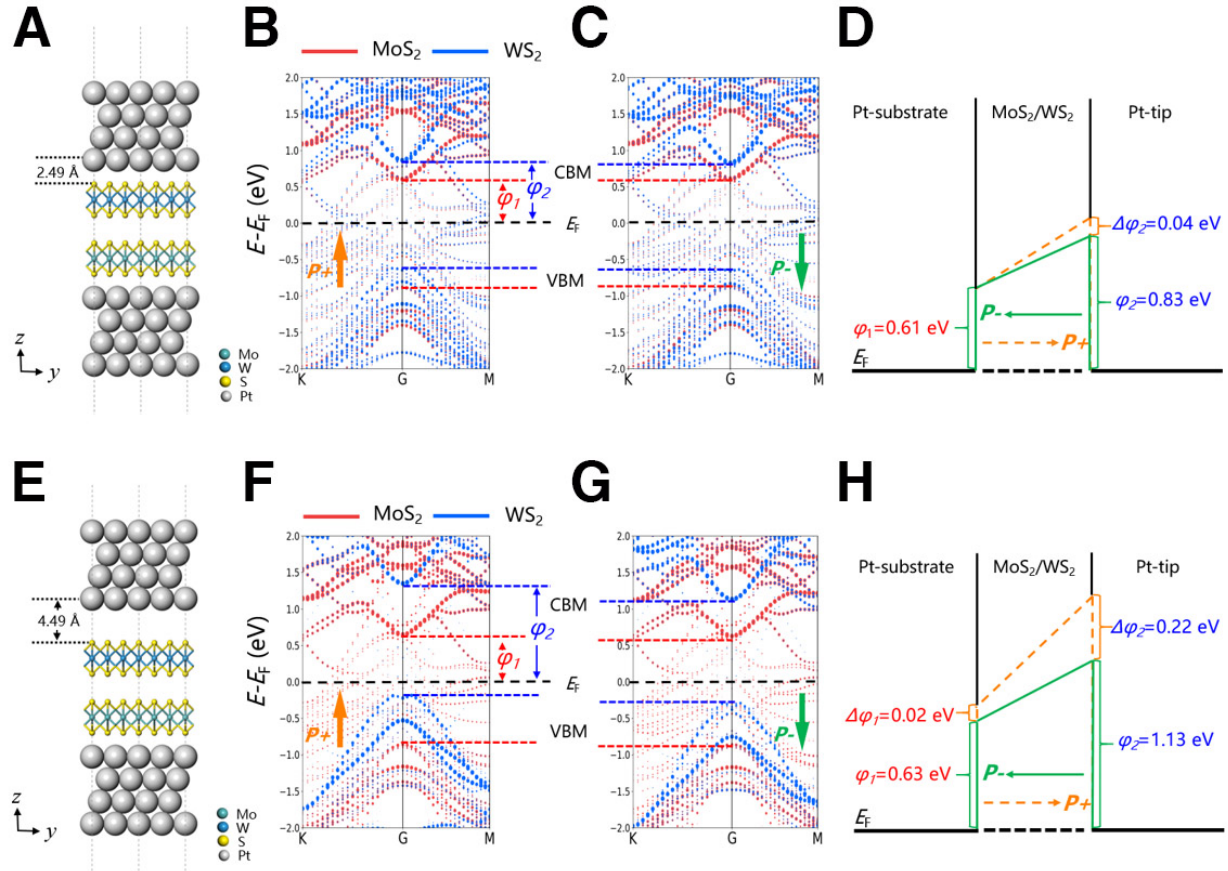# Section 11: Model of ferroelectric tunneling junctions

Fig. S11. Modeling of the Pt-MoS$_2$/WS$_2$-Pt FTJ in the SH (**A**-**D**) and WI (**E**-**H**) cases. Side views of the atomic structure for a dual-slab model for the Pt-MoS$_2$/WS$_2$-Pt heterostructure in the SH (A) and WI (E) cases. The bottom (top) slab represents the Pt (Pt/Ir) substrate (tip). Cyan, blue, yellow and silvery balls represent Mo, W, S and Pt atoms, respectively. Projected band structures of the heterostructures with up (B, F) and down (C, G) polarization directions in the SH (B, C) and WI (F, G) cases. Red and blue colour dash lines indicate the weight of projections of electronic states on the MoS$_2$ and WS$_2$ sites, respectively. The Fermi level is denoted by a black dash line. Energy φ_1 (φ_2) denotes the energy difference between the conduction band minimum (CBM) and the Fermi level, known as the Schottky barrier height for electrons, of MoS$_2$ (WS$_2$). We have darwn the corresponding schematic potential energy profiles with up (orange) and down (green) polarization directions in the SH (D) and WI (H) cases. $\Delta\varphi$ denotes the barrier height difference after reversing the polarization direction.

A dual-slab model was used in fully modelling the FTJ which contains the MoS$_2$/WS$_2$ bilayer, sandwiched by two four-layer-thick Pt slabs, and a vacuum layer (see Fig. S11(A)). The strong hybridization (SH) case at the equilibrium tip-bilayer distance aside, we also considered a FTJ

50

model with a 2 Å-larger tip-bilayer separation to model a weaker interaction (WI) case (Fig. S11(E)) which most likely occurred during our AFM measurements.

All our bandstructures indicate type-II band alignments for the two models with two polarization directions (Fig. S11(B, C) and S11(F, G). In comparison with the projected bandstructures on MoS_2, WS_2 and Pt, we found that the VBs and CBs of MoS_2 and WS_2 were pinned by the Pt slab on either sample or tip side through strong Pt-MoS_2 and WS_2-Pt hybridization in the SH (equilibrium) model. According to the definition of the Schottky barrier height, we could derive φ_1 (MoS_2) and φ_2 (WS_2) from the bandstructures. This strong Fermi level pinning effect also explains a small change of $\Delta\varphi_2$ (~ 0.04 eV) after reversing the interfacial polarization direction (Fig. S11(D)).

In terms of the WI model, the AFM tip was pulled 2 Å away from the bilayer, enlarging the tip-bilayer separation to 4.49 Å (Figure S11(E)), which is more realistic since the tip does not strongly hybridize with the bilayer during the measurements. In this model, while the VB and CB of MoS_2 are still pinned by the Pt substrate, those of WS_2 are less affected by the tip. Thus, $\Delta\varphi_2$ enlarges to ~ 0.20 eV upon the reversal of the interfacial polarization direction (Fig. S11(H)). These values are highly comparable with previously published FTJ research on $BaTiO_3$, where a barrier height change $\Delta\varphi$ of 0.16 eV was reported.(*62*)

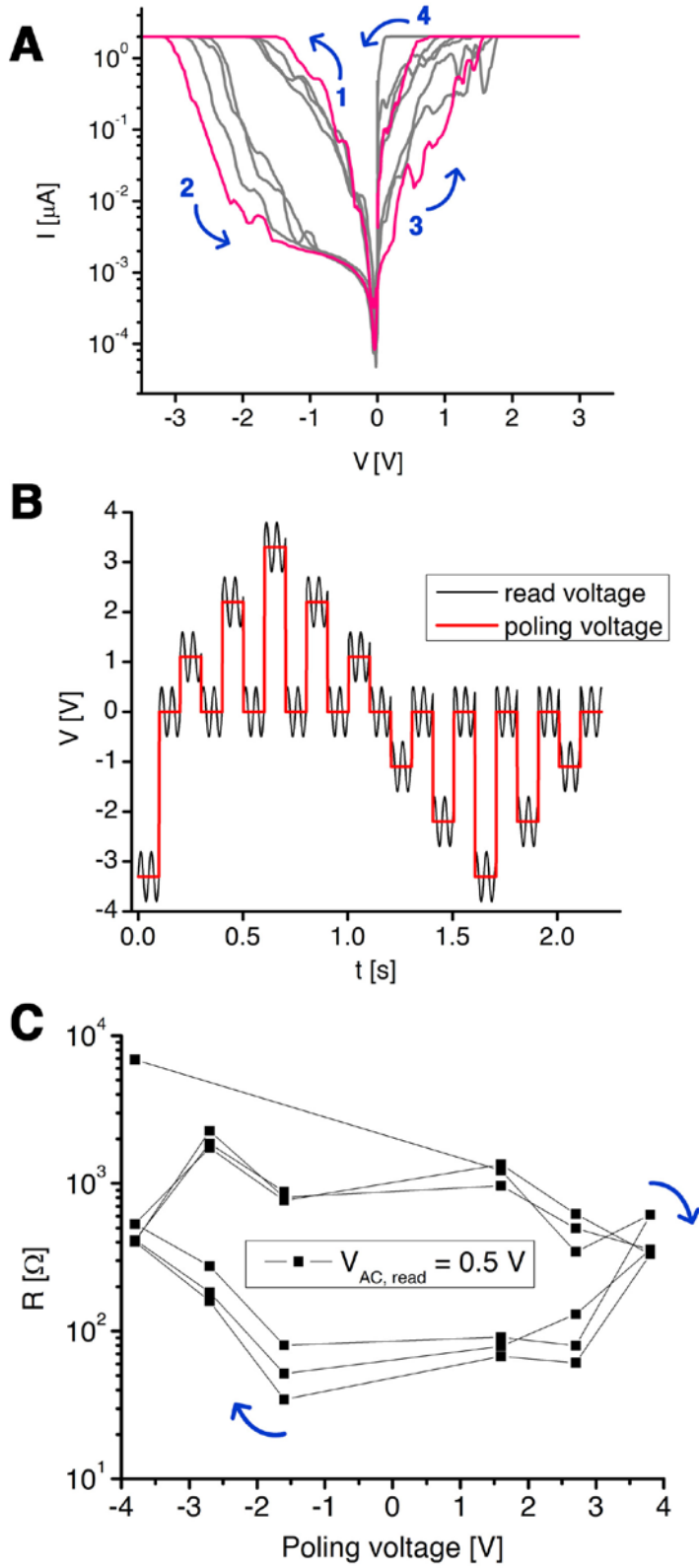*Section 12: Further FTJ measurements.*

Fig. S12. Additional FTJ hysteresis tests. (**A**) Repeated negative poling at -3.5 V and positive poling at +3.0 V on the same spot of an MoS_2/WS_2 heterobilayer sample. The corresponding semi-logarithmic I-V plot is shown. A single full loop was highlighted in magenta. The arrows indicate the direction of the current change. (**B**) ON/OFF resistance switching voltage programme applied to another FTJ device based on our heterobilayer. The square shaped DC poling voltage function and the sinusoidal AC read-voltage were applied simultaneously. The resulting change in tunneling resistance R after each DC poling pulse is shown in (**C**). The arrows indicate the direction of the resistance change. Positive poling reduces resistance; negative poling increases resistance.

We have performed repeated switching between HRS and LRS of our FTJ at a single spot as shown in the semi-logarithmic plot in Figure S12(A). The LRS is activated with a +3.0 V voltage sweep, the HRS state follows a negative -3.5 V sweep. The arrows in the Figure indicate the direction of the current loop throughout the repeated switching process. Just as with the PFM hysteresis, it is also worth considering electrostrictive influences that might obscure our FTJ analysis. Accordingly, we have employed the same ON/OFF method that we used during the DART-SS-PFM hysteresis measurement (see Methods section) to another FTJ device. The voltage function used here is shown in Figure S12(B). The positive and negative DC poling voltages have magnitudes of 1.1 V, 2.2 V and 3.3 V. At the same time a constant AC voltage of 0.5 V magnitude is employed as read-voltage. In-between poling pulses only the read-voltage is active. We have plotted the corresponding tunneling resistance R for the $V_{DC} = 0$ states after each poling pulse in Figure S12(C). The device was pre-poled once with -3.5 V before entering this ON/OFF programme. We can see that the first measurement after pre-poling has a large tunneling resistance, however afterward we can see R entering a loop that nicely shows the HRS and LRS switching after surpassing the coercive voltage points. This test also shows how the poling-induced ferroelectric switching can be read from the device even at low read-voltages and without the impact of major electrostriction.

Section 13: Tensor representation of piezoelectricity and Group Theory.

Any crystal location can be described by a vector $r = \begin{pmatrix} x \\ y \\ z \end{pmatrix}$. Whenever the crystal lattice is moved

around in some way, the coordinate transformation $\begin{pmatrix} x_0 \\ y_0 \\ z_0 \end{pmatrix} \rightarrow \begin{pmatrix} x_1 \\ y_1 \\ z_1 \end{pmatrix}$ can be described by an

appropriate transformation tensor, i.e. a 3x3 matrix with respect to r. There is a special set of

transformations that virtually do not change a crystal lattice in space, they are effectively identity

operations. For example, a carbon atom might be replaced by another carbon atom with the exact

same type of bonds and orientation, which makes the crystal before and after the transformation

indistinguishable. The set of all these special identity operations form a group, called a point group.

The name point group includes that all these transformations are performed relative to a certain

point in the crystal lattice, which for the calculations acts temporarily as the coordinate origin.

Different crystals can belong to different point groups. A group has a number of properties that

will be important to this discussion.(*63*) Groups are closed, which means that the product (i.e. the

subsequent application of) two elements of the group is also an element of the group. This is very

intuitive. Clearly, if a crystal is left invariant by two operations individually, then it is also left

invariant by applying both in sequence. A group always contains the universal identity operation I.

For 3D crystal transformations this is represented by a simple identity matrix.

$$I = \begin{pmatrix} 1 & 0 & 0 \\ 0 & 1 & 0 \\ 0 & 0 & 1 \end{pmatrix}$$

Every group element has an inverse operator that is also necessarily an element of the group.

Multiplying both these elements results simply in I. An example would be to rotate the crystal

clockwise by $60°$ and then again counter-clockwise by $60°$. Lastly, the group elements are

associative. That means that for some general group elements M_1, M_2 and M_3 the

equation $(M_1 M_2) M_3 = M_1 (M_2 M_3)$ is true. In piezoelectricity and SHG research the inversion operation i is probably the most important. The operation can be written as

$$i = \begin{pmatrix} -1 & 0 & 0 \\ 0 & -1 & 0 \\ 0 & 0 & -1 \end{pmatrix} = -I.$$

A very useful deconstruction should be mentioned at this point that can help along when reading the international point group notation (i.e. the Hermann-Mauguin notation). The inversion operation can be rewritten as follows.

$$i = \begin{pmatrix} -1 & 0 & 0 \\ 0 & -1 & 0 \\ 0 & 0 & -1 \end{pmatrix} = \begin{pmatrix} 1 & 0 & 0 \\ 0 & 1 & 0 \\ 0 & 0 & -1 \end{pmatrix} \begin{pmatrix} -1 & 0 & 0 \\ 0 & -1 & 0 \\ 0 & 0 & 1 \end{pmatrix} = m[z] C_2[z]$$

The tensors $m[z]$ and $C_2[z]$ represent a mirror operation perpendicular/normal to the z-axis and a 2-fold rotation (i.e. 180°) around the z-axis. The choice of the z-axis was arbitrary and any random axis could be chosen with the appropriate tensors, including the x-axis and y-axis. In general, a mirror plane will going forward be denoted by a lowercase m and a proper rotation will be denoted by C_n. The index n indicates the degree of rotation via $\theta = \frac{360°}{n}$; for example C_4 is a rotation by $\theta = 90°$ and called a 4-fold rotation. There is a special name when a proper rotation followed by an inversion is performed. These operations are called improper rotations and defined by the relationship $i C_n$. In international notation improper rotation axes are represented by $\bar{n}$, i.e. the rotation index with a bar on top.

In Figure 4(A), a schematic model for bilayer 2H MoS$_2$ is shown. To understand the piezoelectric character of a crystal it is vital to identify its crystal symmetries to properly assign the correct point group to it. We can find for bilayer 2H MoS$_2$ that $C_3[z]$, i.e. a 120° rotation around the z-axis, is a symmetry transformation. In general, the tensor $C_n[z]$ is represented(64) in matrix form by

$$C_n[z] = \begin{pmatrix} \cos(360°/n) & -\sin(360°/n) & 0 \\ \sin(360°/n) & \cos(360°/n) & 0 \\ 0 & 0 & 1 \end{pmatrix}$$

and thus a 3-fold rotation around the z-axis becomes

$$C_3[z] = \begin{pmatrix} -1/2 & -\sqrt{3}/2 & 0 \\ \sqrt{3}/2 & -1/2 & 0 \\ 0 & 0 & 1 \end{pmatrix}.$$

Further, the crystal lattice has $C_2[x]$ and $m[x]$ as two individual identity operations. Our model is arranged such that the x-axis and the zig-zag direction coincide. Another paper might choose differently, but that does not change the fact that the mirror plane is perpendicular to the zig-zag direction in each case. The crystal lattice also has an inversion center, which is a point in space through which an inversion operation would leave the crystal lattice unchanged. The existence of this inversion center disqualifies this crystal for both SHG and piezoelectric measurements entirely. On a side note, the inversion center is also generated by the other group members. As mentioned before, the product of two group elements is also a group element because groups are closed. When $C_2[x]$ and $m[x]$ are multiplied, we get the inversion operation.

$$m[x]C_2[x] = \begin{pmatrix} -1 & 0 & 0 \\ 0 & 1 & 0 \\ 0 & 0 & 1 \end{pmatrix}\begin{pmatrix} 1 & 0 & 0 \\ 0 & -1 & 0 \\ 0 & 0 & -1 \end{pmatrix} = \begin{pmatrix} -1 & 0 & 0 \\ 0 & -1 & 0 \\ 0 & 0 & -1 \end{pmatrix} = i$$

This is a useful tool for crystal symmetry in general. The existence of a 2-fold rotation axis and a mirror plane perpendicular to the same axis generates necessarily an inversion center. However, this does not work in reverse, an inversion center does not imply that either a specific 2-fold rotation axis or mirror plane independently exists as group members. Bilayer 2H MoS₂ belongs to the $\bar{3}\frac{2}{m}$ point group. The symbol $\frac{2}{m}$ implies a 2-fold rotation axis and a mirror plane perpendicular to it, which necessarily generates i, which is a transformation independent of any axis. The

symbol $\bar{3}$ comes about from the tensor multiplication of $C_3[z]$ and i. In international notation, whenever both 3 and $\bar{3}$ are applicable, then the latter is written.

In Figure 4(B), we show the schematic structure of 2H-like MoS₂/WS₂ heterobilayer. The crystal is nearly the same as bilayer 2H MoS₂, except that the transition metal in the bottom layer is W instead of Mo. This has a great impact on the crystal symmetry of the combined crystal. In short, all symmetry operations of bilayer 2H MoS₂ that move atoms from the top to the bottom (and vice versa) become invalid as identity operations, which in this case are $C_2[x]$ and i. The other two symmetry operations $C_3[z]$ and $m[x]$ remain valid. These are precisely the two symmetry operations that land this heterostructure in the $3m$ point group. In essence, the OOP symmetry of bilayer 2H MoS₂ has been broken and this is precisely why OOP piezoelectricity is to be expected from this crystal. In Figure 4(C) we also display 3R-like MoS₂/WS₂ heterobilayer. It has the same symmetry operations as its pure counterpart 3R MoS₂, without the need to invalidate the OOP symmetry as there was not any OOP symmetry to begin with. Both 3R MoS₂ and 3R-like MoS₂/WS₂ are not symmetric in the OOP direction and have an intrinsic OOP polarization.

As mentioned before, piezoelectricity is strongly dependent on crystal symmetry because it relies on intrinsic polarizations. Any monolayer TMDC for instance that belongs to the $\bar{6}m2$ point group does not have an intrinsic OOP polarization. This is due to the existence of an $m[z]$ mirror plane that lies within the plane of the transition metals. There is, however, an intrinsic IP polarization in that crystal and therefore IP piezoelectric effects are to be expected(*65*) and have been measured experimentally.(*66*) For PFM measurements, the inverse piezoelectric effect is exploited and hence we will here consider the equation for it. For $\bar{6}m2$ point group crystals the appropriate equation is as follows.(*4*)

$$
\begin{pmatrix} S_1 \\ S_2 \\ S_3 \\ S_4 \\ S_5 \\ S_6 \end{pmatrix} = \begin{pmatrix} d_{11} & 0 & 0 \\ -d_{11} & 0 & 0 \\ 0 & 0 & 0 \\ 0 & 0 & 0 \\ 0 & 0 & 0 \\ 0 & -2d_{11} & 0 \end{pmatrix} \begin{pmatrix} E_1 \\ E_2 \\ E_3 \end{pmatrix}
$$

Here the vector S_l represents the induced piezoelectric strain created by the external electric field vector E_i. Note that the indices 1, 2 and 3 represent the strain and electric field components along the x-, y-, and z-axis, respectively. S_4, S_5 and S_6 are the shear strains around the x-, y-, and z-axis, respectively. d_{il} are the piezoelectric tensor components. For monolayer TMDCs the first row of the tensor represents the strain in the armchair direction S_1 that is proportional to the electric field component E_1 along the same axis and independent from the other electric field components, E_2 and E_3.(66) The strain S_2 along the zig-zag direction is of the same magnitude but with a negative sign, meaning that an expansion along the armchair direction results in a compression of equal magnitude in the zig-zag direction, and vice versa.

$$
S_1 = d_{11}E_1 \text{ and } S_2 = -d_{11}E_2
$$

Note that the third row of d_{il} is entirely zeroes, meaning that there is no OOP strain S_3 created in any way for monolayer TMDCs, just as we have concluded from the crystal symmetry group.

The piezoelectric tensor for the $3m$ point group is given by

$$
\begin{pmatrix} S_1 \\ S_2 \\ S_3 \\ S_4 \\ S_5 \\ S_6 \end{pmatrix} = \begin{pmatrix} 0 & -d_{22} & d_{31} \\ 0 & d_{22} & d_{31} \\ 0 & 0 & d_{33} \\ 0 & d_{24} & 0 \\ d_{24} & 0 & 0 \\ -2d_{22} & 0 & 0 \end{pmatrix} \begin{pmatrix} E_1 \\ E_2 \\ E_3 \end{pmatrix}
$$

The d_{il} tensor has 4 independent variables and is generally more complex than that of a monolayer TMDC. Note also that the third row is not all zeroes. Instead, we get the linear relationship $S_3 = d_{33}E_3$. We have thus a non-zero OOP piezoelectric component due to the

lacking OOP symmetry discussed above. We have confirmed this relationship experimentally, as shown in the experimental section.

In summary, we have shown herein that 2D heterobilayers deserve their own crystal symmetry considerations, independent of their individual parts. As much as bilayer 2H MoS_2 and 3R MoS_2 each belong to a different point group that is also different from monolayer MoS_2, the same is true for MoS_2/WS_2 heterobilayer.

Section 14: Derivation of the strain piezoelectric constant tensor.

Stress and strain piezoelectric constants are represented by $e_{ijk} = \partial P_i/\partial S_{jk} = -\partial T_{jk}/\partial E_i$ and

$d_{ijk} = \partial P_i/\partial T_{jk} = \partial S_{jk}/\partial E_i$ respectively. Here, P_i and E_i represent the polarization and

macroscopic electric field, while stress and strain are denoted by second-order tensors T_{jk} and S_{jk},

respecitvley.(*67*) Subscripts *i, j, k* ∈ (1, 2, 3) correspond to the spatial *x*- (armchair), *y*- (zig-zag),

and *z*- (vertical) directions, respectively. In the Voigt notation,(*51*) e_{ijk} and d_{ijk} reduce to e_{il} and d_{il},

respectively, where *l* ∈ (1, 2, 3, …,6).

Strain piezoelectric constant tensor d_{il} is related to stress piezoelectric constant *eil* through

elastic constant C_{kl}, *i.e.* $d = eC^{-1}$, where *C* and *e* are directly computable using our DFT methods.

Units of e_{il}, d_{il} and C_{kl} are in C/m², pm/V, and GPa in 3D structures, respectively.

The elastic constants are calculated by fitting the energy-strain curves(*51*), the total energy of

the system by applying small strain vector $\boldsymbol{S} = (S_1, S_2, S_3, S_4, S_5, S_6)$ can be expanded by the Taylor

series $\Delta E = \frac{V}{2}\sum_{i=1}^{6}\sum_{j=1}^{6} C_{ij}S_iS_j$ where *ΔE* is the total energy increment by the small strain vector

S, and *C* is the matrix of elastic constant, and *V* is the effective volume of the equilibrium layered

materials. The effective volume is defined as *V=Area×h_eff*, where *Area* represents the cross

sectional area of cells and h_{eff} is the effective thickness, respectively. The latter quantity can be

evaluated using charge distribution along the *z* direction. We take the position of zero charge

distribution as the boundary of these layered materials.

The lattice vectors of a cell are transformed to the new vectors under the strain by

$$\begin{pmatrix} \boldsymbol{a}' \\ \boldsymbol{b}' \\ \boldsymbol{c}' \end{pmatrix} = \begin{pmatrix} \boldsymbol{a} \\ \boldsymbol{b} \\ \boldsymbol{c} \end{pmatrix} \cdot (I + S)$$

where *S* is the strain tensor

$$S = \begin{pmatrix} S_1 & \frac{S_6}{2} & \frac{S_5}{2} \\ \frac{S_6}{2} & S_2 & \frac{S_4}{2} \\ S_5 & \frac{S_4}{2} & S_3 \end{pmatrix}$$

For the 3m point group, there are four independent elastic constants to derive the z-elements of the d matrix, i.e. C_{11}, C_{12}, C_{13} and C_{33} are thus calculated manually using the following equations.

$$\frac{\Delta E}{V} = (C_{11} + C_{12})S^2 \text{ with applied strain } \boldsymbol{S} = (S, S, 0, 0, 0, 0)$$

$$\frac{\Delta E}{V} = \frac{1}{4}(C_{11} - C_{12})S^2 \text{ with applied strain } \boldsymbol{S} = (0, 0, 0, 0, 0, S)$$

$$\frac{\Delta E}{V} = \frac{1}{2}C_{33}S^2 \text{ with applied strain } \boldsymbol{S} = (0, 0, S, 0, 0, 0)$$

$$\frac{\Delta E}{V} = (C_{11} + C_{12} + 2C_{13} + C_{33}/2)S^2 \text{ with applied strain } \boldsymbol{S} = (S, S, S, 0, 0, 0)$$

Both the e and C matrices[8] could be simplified to

$$e = \begin{pmatrix} e_{11} & -e_{11} & 0 & 0 & e_{15} & 0 \\ 0 & 0 & 0 & e_{15} & 0 & -e_{11}/2 \\ e_{31} & e_{31} & e_{33} & 0 & 0 & 0 \end{pmatrix} \text{ and}$$

$$C = \begin{pmatrix} C_{11} & C_{12} & C_{13} & 0 & 0 & 0 \\ C_{12} & C_{11} & C_{13} & 0 & 0 & 0 \\ C_{13} & C_{13} & C_{33} & 0 & 0 & 0 \\ 0 & 0 & 0 & C_{44} & 0 & 0 \\ 0 & 0 & 0 & 0 & C_{44} & 0 \\ 0 & 0 & 0 & 0 & 0 & (C_{11} - C_{12})/2 \end{pmatrix},$$

Using the relation $d=eC^{-1}$ to derive the OOP strain piezoelectric constant as $d_{33} = [(C_{11} + C_{12})e_{33} - 2C_{13}e_{31}]/[(C_{11} + C_{12})C_{33} - 2C_{13}^2]$.

Type of Layers	C_{11}	C_{12}	C_{13}	C_{33}	e_{33}	e_{31}	d_{33} (pmV^{-1})	
	(GPa)				(C/m^2)		DFT	PFM
2H MoS$_2$ (Bulk)	236.2	57.8	16.1	55.1	0.00	0.00	0.00	0.00
2H MoS$_2$ (expt.(**68**))	238.0	54.0	23.0	52.0	-	-	-	-
2H-like MoS$_2$/WS$_2$	290.8	65.4	21.4	63.4	0.37	1.91	2.28	1.95
3R-like MoS$_2$/WS$_2$	292.7	65.2	27.3	55.9	0.42	1.91	2.40	2.09

Table S1. Theoretical elastic constants(C), piezoelectric stress (e) and strain (d) constants of bulk MoS$_2$ and MoS$_2$/WS$_2$ heterobilayers. Here, C_{11} and C_{12} are IP elastic constants representing stress in the x- and y-directions, respectively, under a strain applied along x; C_{33} and C_{13} are OOP elastic constants and the subscript 3 denotes the z-direction. The OOP piezoelectric stress constants e_{33} and e_{31} record the piezoelectric response under strains applied in the z- and x-directions, respectively, while d_{33} is the OOP piezoelectric strain constant.

Table S1 shows all relevant parameter values needed for deriving d_{33} of our two heterobilayers.

Theoretical elastic constants C_{11}, C_{12}, C_{13} (C_{31}) and C_{33} of the 2H-like heterobilayer are 290.8,

65.4, 21.4 and 63.4 GPa, respectively, which are very close to those of bulk 2H MoS$_2$ as

previously reported experimentally and theoretically.(*68, 69*) A uniform strain in a certain

direction was imposed to the 2H-like heterobilayer supercell for calculating its stress

piezoelectric constants e_{33} and e_{31}. These two constants were obtained by fitting the changes of

electrical polarization with respect to the applied strain, as described in the Methods section,

which yields 0.368 and 1.908 C/m^2 for e_{33} and e_{31}, respectively.

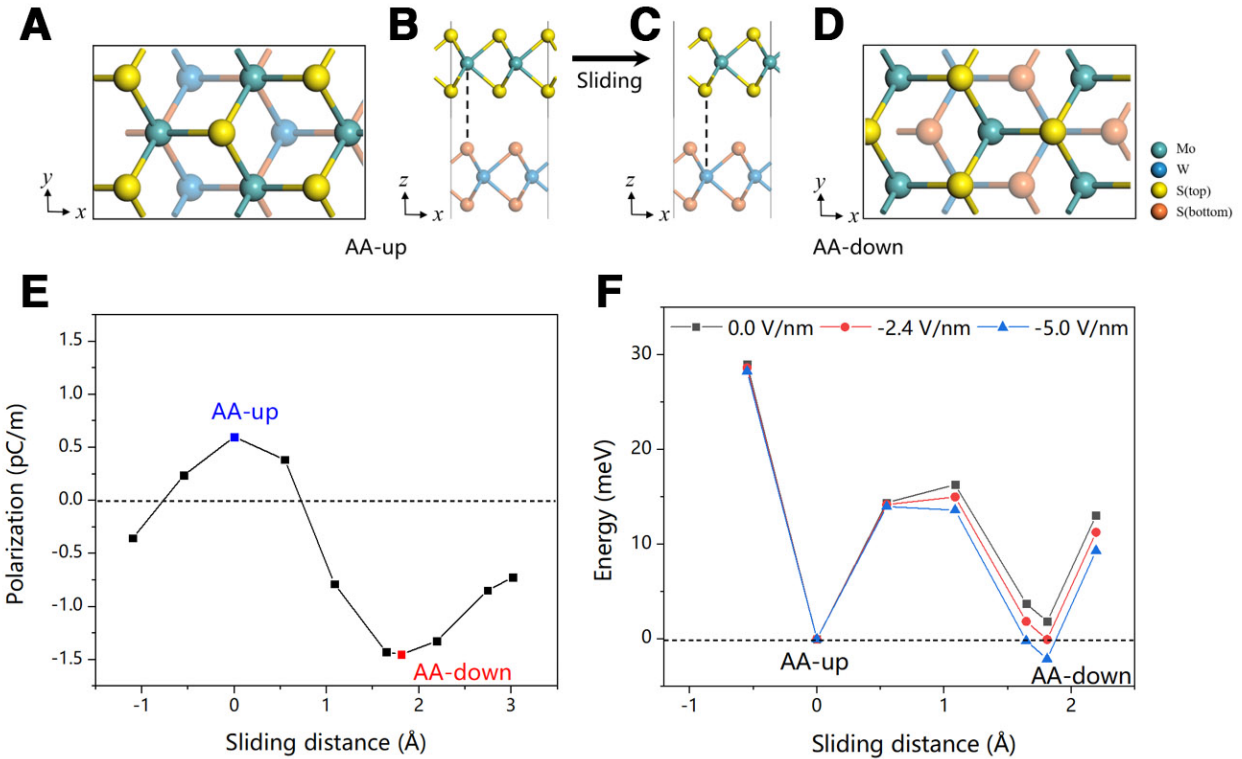*Section 15: Ferroelectric switching behavior in the heterobilayers.*

Fig. S13. Ferroelectric behavior of the 3R-like MoS_2/WS_2 heterobilayer enabled by interlayer sliding. (**A, B**) Top and side views of the initial 3R-like stacking order (AA-up) where a top-layer Mo atom sits over an interfacial S atom of the bottom layer. The cyan, blue, yellow and orange balls represent Mo, W, top S and bottom S atoms, respectively. A lateral sliding of the top-layer along the armchair direction leads to stacking order AA-down, the top and side views of which were displayed in side (**C**) and top (**D**), in which the bottom-layer W atom resides right to blow the interfacial S atom of the top-layer. They have very closed energies as they share the same stacking feature, i.e. metal superposing with interfacial S atoms. (**E**) The spontaneous OOP polarization value varies as a function of the sliding distance. Here, a positive value indicates the polarization pointing to the positive z direction and *vice versa*. The largest positive and negative polarization values were found at $x = 0.00$ Å (AA-up, 0.60 pC·m^{-1}) and $x = 1.63$ Å (AA-down, -1.45 pC·m^{-1}), respectively. (**F**) Relative energy profiles between configurations AA-up and AA-down under zero and finite external electric fields. The appearance of those double-well potentials where those two configurations reside at the well bottom, together with reversed polarization directions, indicate ferroelectricity of the heterobilayer. Configuration AA-up is 1.9 meV/f.u. more

stable than configuration AA-down. The relative stability reverses under an electrical field over 2.4 V/nm being applied to the anti-parallel direction of the polarization, and a field of 5.0 V/nm further stabilizes configuration AA-down energetically by 2.1 meV.

Section 16: PS transfer method.

All transfers for our experiments were executed via a polystyrene (PS) transfer method.(*36*) A solution of 11 g polystyrene per 100 ml toluene is dropped onto the as-grown composite. Subsequently the substrate is spin-coated with 500 rpm for 6 seconds, followed by 3500 rpm for 60 seconds. Next the substrate is to be baked at 70 °C for 15 minutes and then at 90 °C for another 15 minutes. After the baking the edge of the PS-covered substrate would be brought in contact with a DI water droplet and slightly poked with tweezers. The poking will create a small opening between the SiO_2 substrate and the PS cover, which allows for water to penetrate between them and eventually separate them. The composite material is now on the bottom side of the loose PS sheet floating atop the water droplet, which can be removed simply with tweezers and placed on the new target substrate. The new substrate must then be baked again at 105 °C for about 15 minutes to connect the composite with the new substrate. After baking, the substrate is to be immersed in toluene for about 10 minutes, after which it should be immersed into a second toluene bath for a few hours. After the etching period, the sample should be lifted out of the toluene bath horizontally, such that a film of toluene remains on top. This remainder should then be blown off quickly with an air gun or nitrogen gun. This last step should not be omitted or else large residues might remain on the surface.